Nano Research

ISSN 1998-0124 CN 11-5974/O4
https://doi.org/10.1007/s12274-021-3546-1

Flagship Review

Adaptive iron-based magnetic nanomaterials of high performance for biomedical applications

Ning Gu[1,2,3] (✉), Zuoheng Zhang[1,2], and Yan Li[1,2]

[1] *State Key Laboratory of Bioelectronics, Jiangsu Key Laboratory for Biomaterials and Devices, School of Biological Science and Medical Engineering, Southeast University, Nanjing 210096, China*
[2] *Collaborative Innovation Center of Suzhou Nano-Science and Technology, Suzhou Key Laboratory of Biomaterials and Technologies, Suzhou 215123, China*
[3] *School of Biomedical Engineering and Informatics, Nanjing Medical University, Nanjing 211166, China*

Received: 11 February 2021 / **Revised:** 14 April 2021 / **Accepted:** 27 April 2021

ABSTRACT

With unique physicochemical properties and biological effects, magnetic nanomaterials (MNMs) play a crucial role in the biomedical field. In particular, magnetic iron oxide nanoparticles (MIONPs) are approved by the United States Food and Drug Administration (FDA) for clinical applications at present due to their low toxicity, biocompatibility, and biodegradability. Despite the unarguable effectiveness, massive space for improving such materials' performance still needs to be filled. Recently, many efforts have been devoted to improving the preparation methods based on the materials' biosafety. Besides, researchers have successfully regulated the performance of magnetic nanoparticles (MNPs) by changing their sizes, morphologies, compositions; or by aggregating as-synthesized MNPs in an orderly arrangement to meet various clinical requirements. The rise of cloud computing and artificial intelligence techniques provides novel ways for fast material characterization, automated data analysis, and mechanism demonstration. In this review, we summarized the studies that focused on the preparation routes and performance regulations of high-quality MNPs, and their special properties applied in biomedical detection, diagnosis, and treatment. At the same time, the future development of MNMs was also discussed.

KEYWORDS

magnetic nanomaterials, high performance, performance regulation, controllable assembly, biomedical applications

1 Introduction

Magnetic nanomaterials (MNMs) have been widely used in the biomedical field, including magnetic resonance imaging (MRI) [1, 2], hyperthermia [3], drug carriers [4, 5], gene delivery [6], biological detection [7], cell labeling [8–10], scaffolds for tissue engineering [11–14], etc. The latest discovery indicated that the magnetic nanoparticles (MNPs) combined with a mild magnetic pulse sequence could rapidly improve the depressive-like symptoms in mice [15]. Commonly, MNMs are based on ferromagnetic transition elements like iron (Fe), cobalt (Co), and nickel (Ni), among which iron is the most abundant essential trace element in the human body that exhibits the best biosafety and participates in many fundamental live activities [16]. Therefore, iron-based MNMs, including pure iron, iron based alloy, iron oxides, and coordination complexes of iron, attracted much more attention than others. In particular, magnetic iron oxide nanoparticles (MIONPs) are approved by the United States Food and Drug Administration (FDA) for clinical application at present [17]. There is still room for improvements in the MNMs, though above-mentioned applications have exhibited their broad prospects in the biomedical field.

As is well known, the biosafety of iron-based MNMs is crucial for biomedical applications. The *in vivo* interaction of MNPs and biological system is quite complicated. MNPs can be distributed into various organs and the following excretion pathway depended on their size. Small MNPs (< 10 nm) are usually rapidly removed through extravasation and renal clearance, whereas larger ones (> 200 nm) are filtered by the spleen and eliminated through the liver [18, 19]. MNPs commonly decompose into free iron after cellular uptake and then incorporated into the body's pool of iron. Iron-based MNPs potentially interfere with physiological iron metabolism [20], decrease the cell viability [21], and increase the gene mutation frequency [22], even if they exhibit much weaker cytotoxicity than other nanomaterials. These types of potential cytotoxicity are dose-dependent. That is, a higher concentration of MNPs would induce more serious side effects [23]. When MNPs are employed in some specific applications, especially in MRI and hyperthermia, they have to maintain sufficient concentration during the clinical procedure to guarantee the imaging quality and therapeutic effect [18]. Therefore, for the sake of minimizing the effective dosage of MNPs in biomedical applications to avoid possible toxicity, it is of vital importance to prepare MNPs with higher magnetism.

To simultaneously acquire good biocompatibility and high quality in MNPs, one should choose the synthetic methods of MNPs and some relevant auxiliary means with great deliberation. The preparation routes for MNPs can be roughly classified

Address correspondence to guning@seu.edu.cn

into aqueous- and organic-phase synthesis according to the types of solvents. For the preparation of clinical MNPs, organic-phase synthesis methods were usually not preferred, because they potentially elevate cytotoxicity due to the complicated reaction systems with various organic reagents [24]. The chemical co-precipitation method, which is the representative one in aqueous solution, can rapidly and easily prepare hydrophilic and biocompatible MNPs on a large scale, as is used in the production of commercially available Feridex© and Resovist© drugs [25]. Unfortunately, it is hard for the chemical co-precipitation method to attain MNPs with narrow particle-size distribution, high crystallinity, and strong magnetism. Therefore, great efforts have been devoted to the preparation of MNPs on the basis of physically assisted strategies [26], as well as artificial intelligence techniques [27] and theoretical calculation [28]. These open up the novel and effective ways of enhancing the performance of MNPs without using extra chemical reagents.

Sometimes, common MNPs could not meet various clinical requirements. For drug delivery, spherical MNPs might not be the best choice due to the shorter blood circulating life [29] and lower active targeting efficiency [30]. Conventional iron-based nanomaterials are generally employed as T_2-MRI negative contrast agent rather than T_1-MRI positive contrast agent, which is preferable for the MRI [2]. It has been demonstrated by previous researches that the performance regulation of MNPs provided a manner to solve the problems mentioned above. On the one hand, through changing individual MNPs' structural features, including sizes [31], morphologies [32], and compositions [33], their MRI contrast effect, magnetothermal effect, and enzyme-like activity could be enhanced or weakened. Particularly, extremely small MIONPs would exhibit stronger T_1-MRI effect favoring MRI diagnostic accuracy and sensitivity. On the other hand, magnetically-assembled aggregations of MNPs with specific arrangements and orientations could reveal distinctive functions, such as orientation-dependent thermogenesis [34], anisotropic mechanical properties [35], ultrasonic response [36], and highly tunable photonic crystals [37]. Naturally, these distinctive functions considerably broadened applications of MNMs in the biomedical field. Compared with dispersed MNPs, magnetic assemblies have higher drug loading capacity [38] and longer blood circulating life [29]. When imbedded in hydrogels, these assemblies can be used as a cell culturing platform to facilitate the spontaneous formation of multicellular spheroids [39]. Coupling MNPs with microbubbles will increase the stability of the latter [40] and can be used as contrast agents for the double-modality (magnetic resonance (MR) and ultrasound (US)) imaging [41]. Hence, above-mentioned exploration about the performance regulation of MNPs also provides new insight for smart drug delivery and theranostic agents.

Therefore, the preparation of MNPs is not only significant to the nanomaterial industry but also fundamentally important for the development of clinical magnetic nano-drug applied in detection, diagnosis, and treatment. The MNPs for biomedical applications are expected to be synthesized without introducing potentially toxic reagents, and to possess narrow particle-size distribution, high crystallinity, and suitable magnetic and physiochemical properties. Moreover, in order to meet the specific clinical requirements, some properties can be enhanced dramatically or some distinctive functions can be revealed via changing individual MNPs' structural features or assembling them in an orderly arrangement. We summarize the efforts on the preparation of high-performance MNPs, the methods and effects of their performance regulation, and the special properties of MNPs for biomedical applications. In the end, the next frontier to further drive the rapid development of MNMs is also pointed out.

2 Preparation of high-performance MNPs

2.1 Improvements in the preparation method assisted by physical methods

The synthesis routes of magnetic iron oxide nanomaterials comprise chemical co-precipitation method [42, 43], high-temperature decomposition method [44, 45], hydrothermal method [46], sol-gel method [47], polyol method [48], micro-emulsion method [49], etc. The chemical co-precipitation and high-temperature decomposition methods are typical preparation ways in aqueous and organic solutions, respectively. In the high-temperature decomposition method, various precursors are added into organic solvents to synthesize monodisperse MIONPs with high crystallinity. Their excellent monodispersity and crystallinity suggest no obvious deficiency in the performance of MNPs [50]. The critical problem of this synthetic method is that the toxicity from various organic compounds in the complex reaction system is introduced inevitably. In order to increase the biocompatibility of as-prepared MNPs, extra organic solvents and more complex procedures are required. By contrast, the chemical co-precipitation technique exhibits the significant advantages of hydrophilicity, biocompatibility, biosafety, mild reaction conditions, and high reaction rates. Feraheme™ prepared by the classic chemical co-precipitation method was approved by the U.S. FDA to treat iron deficiency in patients in June 2009 [17]. Meanwhile, this method is limited due to the following disadvantages: wider particle-size distribution, lower crystallinity, and weaker magnetic property. It is the best way to obtain MNPs with high performance and good biosafety through improving the chemical co-precipitation method with some physical methods rather than extra reagents. Therefore, this review focused on the physically assisted strategies for the chemical co-precipitation method.

The chemical co-precipitation method is carried out in the aqueous solution, and their products are water-dispersive even without complicated coating agents. Massart [51] first put forward the method for the Fe_3O_4 formation based on the hydrolysis and condensation of ferrous and ferric ions. However, Fe_3O_4 nanoparticles are prone to be oxidized to α-Fe_2O_3 under oxygen-abundant conditions, and subsequently lose the magnetic properties. Alternatively, γ-Fe_2O_3 nanoparticles have better chemical stability and similar magnetic properties. They are commonly obtained from ferric nitrate solution at 100 °C by the co-precipitation method [52], but it is necessary that the residual ferric nitrate is washed off after oxidization. In the hope of surmounting the aforementioned shortcomings in both preparation methods, we proposed the aeration oxidization method in which no extra reagent is used, and the purity of the product is improved [43].

The suboptimal performance of MNPs prepared by the classic chemical co-precipitation method might result from the two dominant factors: the coexistence of crystal nucleation and growth processes, and the inhomogeneity of the reaction system (Fig. 1(a)). Some physically-assisted strategies have been developed according to the two dominant factors. For instance, MIONPs were prepared by rapidly injecting iron salts solution and ammonia solution into the refluxing hot polymer aqueous solution [42]. The products exhibited narrow size distribution and high crystallinity because the rapid injection of all the precursors yielded a high supersaturation concentration in a short time to separate the burst nucleation and the growth process. On the other hand, microfluidic reactors were designed

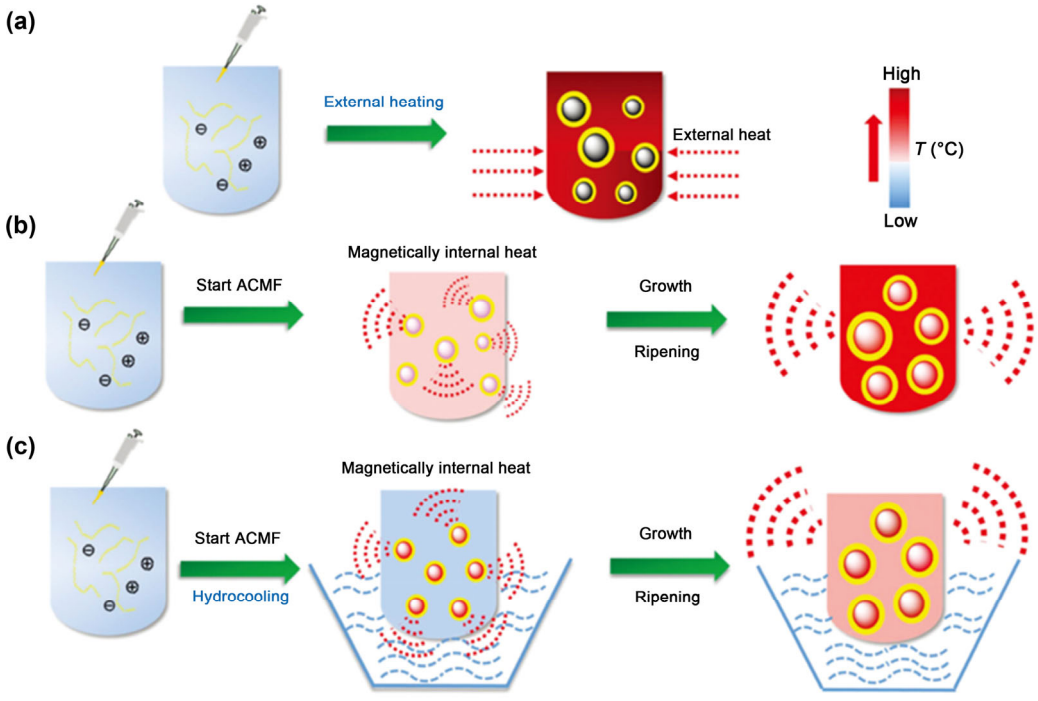

Figure 1 Experimental schematic for the fabrication of MIONPs by (a) ordinary co-precipitation, (b) only ACMF, and (c) coupling hydrocooling and ACMF. (Reprinted with permission from Ref. [26], © Royal Society of Chemistry 2018).

and applied in the preparation of MIONPs to minimize the local concentration and temperature variations in the reaction system [53, 54]. The obtained MIONPs possessed larger saturation magnetization compared with bulk synthesis.

Recently, our group made a series of systematic attempts to improve the performance of MNPs prepared by the chemical co-precipitation method. Firstly, an innovative way of heating induced by alternating-current magnetic field (ACMF) in the co-precipitation reaction to prepare MIONPs or clusters was developed (Fig. 1(b)) [55, 56]. The as-synthesized MIONPs were better in quality than Feraheme™ on particle-size distribution, crystallinity, and magnetism. The magnetic clusters prepared under similar reaction conditions had a better heat generation compared with the clusters with similar sizes by the traditional chemical co-precipitation. Secondly, hydrocooling and magnetically internal heating co-precipitation (HMIHC) was introduced to replace the traditional external heating [26] (Fig. 1(c)). The combination of hydrocooling and magnetically internal heating could regulate the reaction temperatures to easily separate the nucleation and the growth stages. The magnetization of the newly developed nanoparticle reached 104–105 emu/g Fe, which was the highest among the reported results. Thirdly, ACMF was also applied in the preparation of Prussian blue nanoparticles (PBNPs), which exhibited outstanding catalytic performance and MRI contrast efficiency [57]. Moreover, inspired by the ACMF-assisted co-precipitation method, a microwave-assisted high-temperature decomposition procedure was also developed [58, 59]. Monodisperse Fe_3O_4 nanoparticles can be rapidly produced at a lower aging temperature without harsh reaction conditions as in the traditional high-temperature decomposition method.

Furthermore, we also attempted to illustrate the mechanisms of ACMF for the crystal growth in the chemical co-precipitation method [26]. On the one hand, ACMF could cause thermogenesis by the formed seeds to activate the specific growth on the surfaces of these crystal nuclei and to facilitate further self-ripening of the nanocrystal. On the other hand, ACMF could drive the transition of magnetic moment arrangement from a random state to an ordered state, which was proved by using micromagnetic simulation and X-ray magnetic circular dichroism (XMCD) techniques. For the PBNPs, the routes of formation are different from that in ACMF induced by lower or higher current intensity. Small nanocrystals could continuously enlarge, maintaining good crystallinity and smooth surfaces in all crystallization stages at lower current intensity. By contrast, higher current intensity would lead to directional aggregation of small nanoparticles into mesocrystals with more crystal defects at early stages. Then the mesocrystals would be transformed into real single crystals via fusion at the interior of the nanoparticles [57]. The typical non-classical crystallization process somewhat resembles the multistage nucleation and phase transformation mechanisms [60, 61].

Though the aforementioned magnetically internal heating significantly improved the size distribution of nanoparticles in the chemical co-precipitation method, it is still hard to achieve sufficient monodispersity due to the aggregation caused by the intrinsic magnetic interactions. Consequently, a novel high-gradient magnetic separator, composed of a uniform magnetic field and a nanowires array by deposition of Fe [62], was fabricated and applied to optimize the colloidal dispersity [63]. When MNPs suspension flowed through it, the relatively large nanoparticles or clusters would be removed from the suspension so that the size distribution of MNPs gets narrower.

It is noteworthy that the above-mentioned studies that are conducted to improve the performance of MIONPs, including rapid injection, microfluidic reactor, magnetically internal heating, and magnetic separation, are physically assisted strategies. They can avoid the potential toxicity by introducing minimum extra molecules or solvents into the reaction system. Further, the basic physical and chemical properties of ferumoxytol were well retained so as to meet the pharmaceutical quality criteria for clinical use. Magneto-diagnostic/therapeutic devices such as magnetic resonance imaging device and magneto hyperthermia device have been steadily applied in clinics, and there is no doubt the large-scale magnetic field generator will be readily scale-up fabricated in industrial workshop [64]. The

thermogenesis caused by every formed seed under ACMF could be distributed in the whole space homogeneously, even the reaction vessel become larger to obtain a large amount of MNPs. Thanks to the magneto medical device advancing, the magnetically internal heating co-precipitation is promising to realize mass production.

2.2 Characterization analysis and theoretical calculation

In recent years, artificial intelligence and theoretical calculations have developed rapidly. They have been widely used in as-prepared material characterization and related mechanism interpretation to facilitate the exploration of high-quality MNPs (Fig. 2).

Obtaining high-resolution images is fundamental for characterizing MNPs to understand the correlations between their structure and properties, but it is usually hard due to the equipment limitations and environmental impacts. Generative adversarial networks (GANs), as an unsupervised deep learning model, have been applied to enhance the resolution of microscopic images [65, 66]. There are two branches, the generator and the discriminator in the networks. For the sake of image enhancement, the generator tries to reconstruct high-resolution images from low-resolution ones as real as possible, while the discriminator is trained to distinguish which ones are fake. The trained model can induce a two-fold increase in resolution to retrieve the useful features of the materials.

Some novel algorithms were used in the processing of microscopic images to quickly and efficiently characterize nanomaterials in terms of their morphologies [67, 68], sizes [69], particle densities [70], and crystallographic defects [71]. Lately, a method applying a genetic algorithm for mass-throughput analysis of the morphologies of nanoparticles is reported [72]. The proposed method enables the analysis of over 150,000 nanoparticles with a high precision of 99.75%. In the preparation of MIONPs, many crystals are coexisting, such as Fe_3O_4, α-Fe_2O_3, γ-Fe_2O_3, and α-FeOOH [73]. In order to automatically recognize the crystallographic structure of every single nanoparticle from high-resolution transmission electron microscopy (HRTEM) images, deep learning for the quantitative calculation of the relevant lattice spacings and inter-plane angles was applied [27]. The calculated data could then be mapped to a certain crystal through matching with the standard powder diffraction file (Fig. 3). We also proposed a kinetics-based method [74] to quantitatively and quickly evaluate the collective magnetization of colloidal MNPs from image sequences on the basis of the relationship between the magnetic force on a colloidal droplet and the movement of the droplet under a gradient magnetic field. The method was recently extended to the measurement of the magnetic moments of a single viable magnetic mesenchymal stem cell labeled with superparamagnetic iron oxide nanoparticles (SPIONPs) economically and noninvasively [75].

Quantum mechanical (QM) calculation [28, 76, 77], molecular dynamics (MD) simulation [78, 79], and micromagnetics

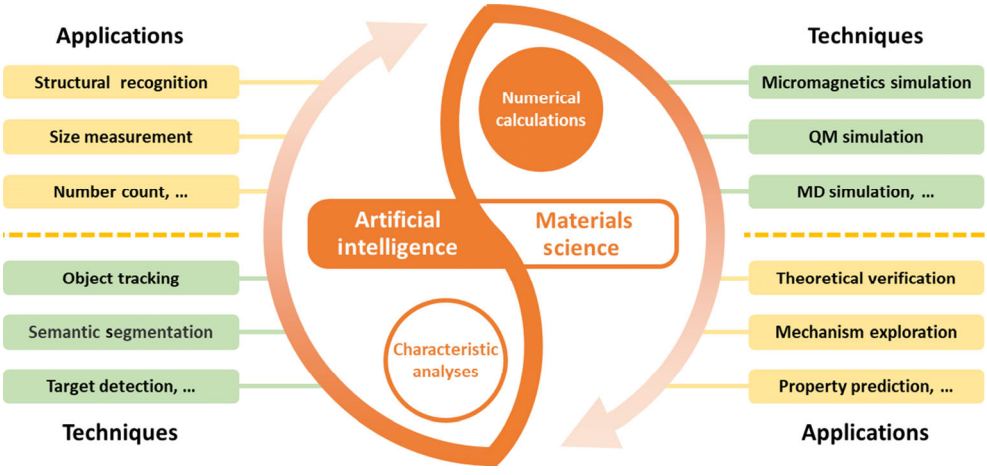

Figure 2 Some key techniques and corresponding applications in the characteristic analyses and numerical calculations based on the combination between artificial intelligence techniques and materials science.

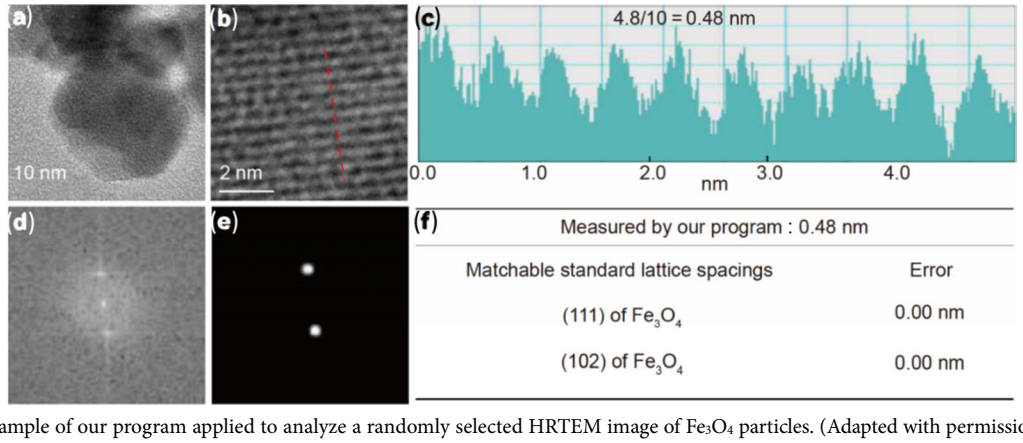

Figure 3 An example of our program applied to analyze a randomly selected HRTEM image of Fe_3O_4 particles. (Adapted with permission from Ref. [27], © Science China Press and Springer-Verlag GmbH Germany, part of Springer Nature 2020). (a) HRTEM image of Fe_3O_4 particles. (b) Zoom-in HRTEM image showing parallel lattice planes. (c) Manual selection and measurement of lattice spacing with Gantan Digital Micrograph software. (d) Fast Fourier transformation image of the image in (b). (e) Spots extracted by our program developed from deep learning. (f) Measured lattice spacing in comparison with standard data.

simulation [26, 59] have been widely used to illustrate the synthetic mechanism of MNPs. Rosso and his co-workers using density functional theory (DFT) calculations studied the adsorption of aqueous Fe^{2+} ions and interfacial electron transfer between adsorbed Fe^{2+} and structural Fe^{3+} at the interface of water–goethite [77] or water–hematite [76]. While, the iron oxide synthesis in the aqueous phase is too complex for DFT simulation due to the unaffordable computational cost. It was observed by alternatively employing MD simulations that some iron-hydroxyl molecular oligomers and amorphous iron oxyhydroxide nanoparticles were formed from the dispersed ions in aqueous without considering the proton transfer between hydroxide ions, which was considered to be the early stage of nucleation of iron oxyhydroxide/oxide nanoparticles [79]. The further deprotonation of hydroxyl ions to form iron oxide was reproduced by Zahn and his group with their original Kawska–Zahn approach [80] and a combined QM/MM approach [81, 82]. These results of MD simulations illustrated the pathway of iron oxide nucleation was nonclassical nucleation [83].

Recently, there is tremendous interest in using machine learning or deep learning techniques to build new alternative models to replace computationally expensive *ab initio* calculations [84]. The interaction between atoms is derived from the carefully crafted artificial neural networks, which can be trained with chemically accurate data from high-level quantum chemistry [85]. These new models based on artificial neural networks can realize high-accuracy simulations in a large time and spatial scale with low computational cost. Moreover, methods through the combination of classical theory and machine learning were applied in the predictions of the shape [86], energy [87], and electron transfer properties [88] of noble metal nanoparticles. They have exhibited promising potential and provided new ideas for the computer-aided designs of MNPs.

Digital image processing, machine vision, and machine learning are being extended at an irresistible pace to the fast measurements, automated analysis, and numerical calculations of crystal nanomaterials. The innovation of computer technology is expected to promote the preparation of high-quality medical MNPs. Exploring new applications of artificial intelligence in materials science will be the primary focuses of future researches.

3 Performance regulation of MNPs

3.1 Performance regulation of individual MNPs

The performance of individual MNPs mostly depend on their sizes [31], morphologies [32, 45], and compositions [89] (Fig. 4). Many explorations on regulating sizes, morphologies, and compositions of MNPs have been made to facilitate their various applications in the healthcare field. How to optimize the performance of MNPs for specific clinical requirements still is a valuable research issue.

3.1.1 *Sizes*

Fe_3O_4 nanoparticles with different diameters could be prepared by adjusting the concentration of the reactant $FeSO_4$ in the aqueous phase [31] or the alkalinity of the reaction system in organic solvents [90]. Recently, fine size control of MIONPs can be easily realized through regulating the molar ratios of various solvents and reaction conditions in the high-temperature decomposition method of iron precursors [59, 91]. On the basis of the as-prepared Fe_3O_4 nanoparticles [31], Yan's group [92] first discovered its intrinsic peroxidase-like activity and validated that the catalysis activity was dependent on the size due to different surface-to-volume ratios to interact with the substrates.

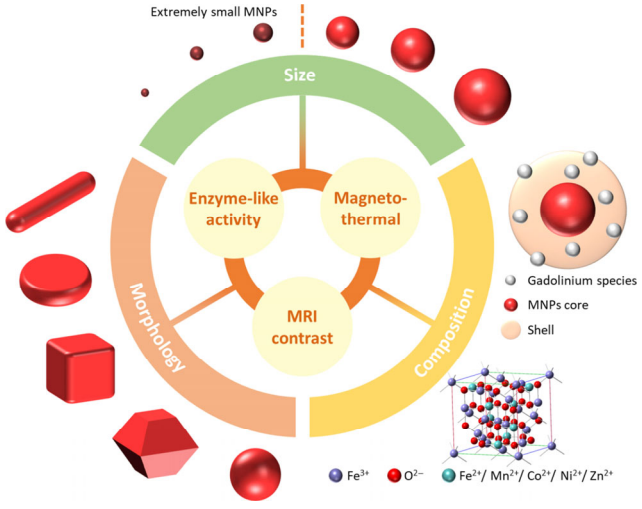

Figure 4 Various performance regulation methods of individual MNPs, and some key factors influenced by the regulation.

Furthermore, our group studied the specific absorption rate (SAR) values and microwave absorption performance of Fe_3O_4 nanoparticles with different diameters [31, 59, 91]. Both of them are strongly size-dependent but have different trends. For larger particles, the SAR values increase as the sizes decrease because the hysteresis loss is the main contribution mechanism. For smaller particles with superparamagnetism, the SAR values and the diameters of particles increase together because relaxation losses, such as Neel loss and Brownian rotation loss, are dominant instead of hysteresis loss. On the contrary, reflection loss (RL) values, which can quantify the microwave absorption performance, increase with increasing size from 4 to 200 nm. The micromagnetic simulation was subsequently performed and the simulation results suggested that coupling interaction and magnetic dipole–dipole interactions between MNPs and electromagnetic field showed synergistic effect to impact the absorption behavior.

In particular, extremely small MIONPs possess unique high T_1-MRI effect [93–95], while conventional iron-based nanomaterials are generally employed as T_2-MRI negative contrast agents, which might be limited in clinical indication expansion by their magnetic susceptibility artifacts. Recently, a moderate cooling co-precipitation method for extremely small MIONPs has been proposed, which could restrict crystal growth after homogeneous nucleation [96]. The as-synthesized extremely small MIONPs displayed around 3-fold higher T_1 MRI signal intensity than that of commercial Ferumoxytol. This characteristic can be attributed to a large number of paramagnetic centers on the surface of nanoprobes and rapid water proton exchange rate (inner sphere model), as well as strong superparamagnetism (outer sphere model) [94]. Extremely small MIONPs displayed significant potential to improve the diagnostic accuracy and sensitivity in MRI and provided an alternative to Gd-based agents.

3.1.2 *Morphologies*

Similar to control of size, adjusting the molar ratios of organic solvents and reaction conditions can also regulate the morphologies of MNPs in the high-temperature decomposition method [32, 45, 97]. Various morphologies of MNPs were synthesized, such as spherical, (quasi-) cubical, rodlike, starlike, platelike and "multibranched" nanocrystals through the above methods. Moreover, a very easy one-pot hydrothermal synthesis

approach was also developed to prepare ultrathin magnetite nanoplates [98]. Introducing ethylene glycol (EG) into the reaction played a critical role in these nanoplates' formation process. The thickness of Fe_3O_4 nanoplates decreases as the concentration of EG increases.

In a traditional crystal nucleation/growth process, the effect of solvents on morphologies might result from the possible differential stabilization of oleic acid (OA) on specific crystal facets which alters relative crystal growth rates. Shortening nucleation duration would bring deficient nucleation and accelerate the subsequent growth process of nanocrystals to form starlike nanocrystals. They were further oriented to assemble reciprocally, gradually forming initial three-dimensional (3D) "branched" nanoclusters to minimize the magnetostatic energy. In addition, the "branched" nanoclusters would transform into the final "multibranched" nanoclusters with sharp or obtuse edges due to the secondary growth in the presence of surface defects and the monomers.

The effect of morphologies is weaker than that of size on the magnetism of nanomaterials. The quasi-cubical shape had stronger saturation magnetization, which accordingly resulted in better MRI contrast and heat conversion efficiency under magnetic induction [45]. In the "multibranched" nanoclusters, sharp-edged nanoclusters, although are larger in size than obtuse-edged nanoclusters, had weaker magnetism. This phenomenon can be attributed to that obtuse-edged nanoclusters had more densely packed structure to increase the magnetic moment [32].

3.1.3 *Compositions*

In order to enhance the signal sensitivity and contrast effect of MRI, MIONPs can be doped with other metallic elements to adjust their composition.

For the T_1 contrast effect, embedding Gd^{3+} ions into MIONPs could exhibit larger r_1 value than that of pure MIONPs due to the interaction between the Gd^{3+} ions and water molecules [99, 100]. Commonly, direct contact between doped Gd^{3+} ions and MNPs should be avoided because the strong magnetic fields caused by T_2 contrast materials resulted in the signal attenuation during T_1 relaxation processes [101].

The magnetic property of Fe_3O_4 nanoparticles is mainly dominated by the magnetic spins of only Fe^{2+} ions in the octahedral sites because the numbers of Fe^{3+} ions in the octahedral/tetrahedral sites are the same, and their magnetic spins cancel each other [102]. Therefore, doping other divalent transition metal ions, such as Mn^{2+}, Co^{2+}, Ni^{2+}, and Zn^{2+} ions in Fe_3O_4 to partially replace Fe^{2+} ions is a common way for controlling the T_2 contrast effect [33, 89, 103]. Among the divalent ions, Mn^{2+} ions could provide the strongest magnetic moment and the $MnFe_2O_4$ possessed the highest r_2 relaxivity (358 $mM^{-1}\cdot s^{-1}$) due to the highest saturation magnetization [104]. It should be noted that the reaction solvent might influence the magnetic properties of $MnFe_2O_4$ nanoparticles. For example, the solvent with stronger reducibility can result in significant improvement in crystallinity and saturation magnetization [105].

3.2 Assembly of MNPs

Collective properties of MNMs are determined by not only the properties of individual nanoparticles, but also the arrangements and orientations in their assemblies. Commonly, in comparison with these individual nanoparticles, assemblies of magnetic nanocrystals could still achieve higher magnetic performance in the absence of harsh apparatus and condition of the reaction [106]. Sometimes, the assembly may even acquire distinctive functions, such as orientation-dependent thermogenesis [34], ultrasonic responsiveness [36], and highly tunable photonic crystals [37]. Following are three categories of assembly discussed in details (Fig. 5), including direct self-assembly, external magnetic field-assisted assembly, and interface induced assembly, which are distinguished based on the driving forces.

3.2.1 *Direct self-assembly of MNPs*

The direct self-assembly of MNPs can be triggered by the van der Waals or electronic interactions between the surface modifiers of neighboring nanoparticles [38, 106–108]. By regulating the agents added into the colloidal solution, the well-dispersed MNPs can aggregate gently into clusters. For

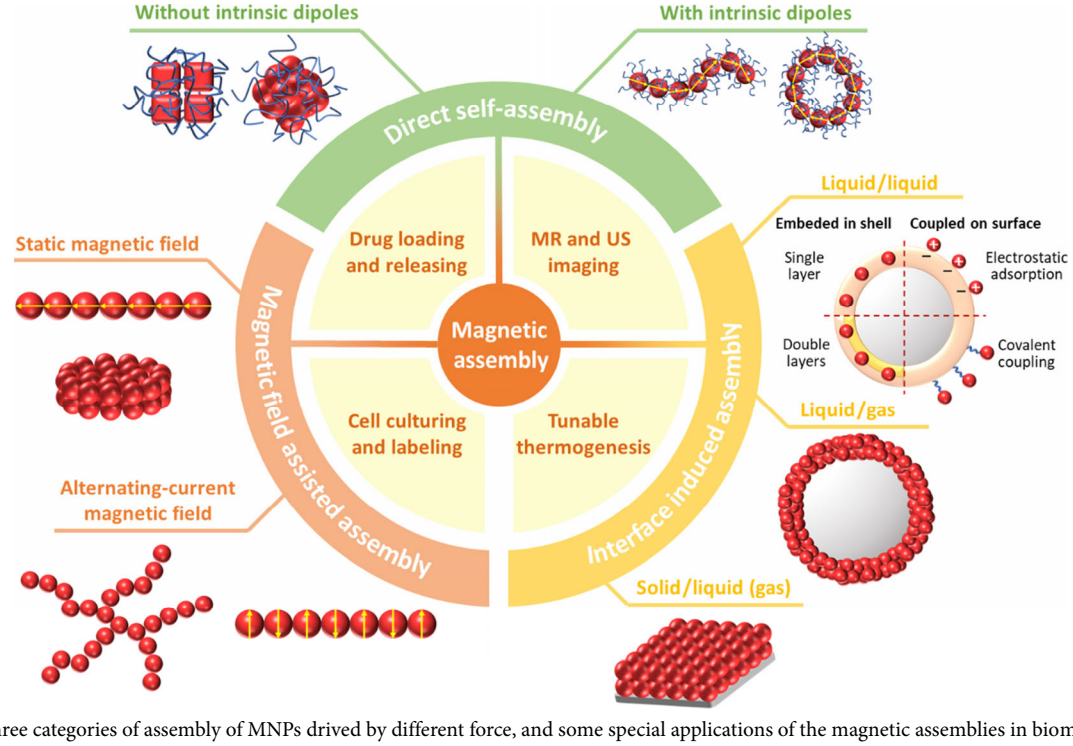

Figure 5 Three categories of assembly of MNPs drived by different force, and some special applications of the magnetic assemblies in biomedical fields.

example, four separate oleic acid-terminated iron oxide nanotubes and oleic acid-modified polyethylene glycol (PEG) molecules were assembled to form clusters during the evaporation of tetrahydrofuran (THF), which was caused by the hydrophobicity of oleic acid in the final aqueous solution [38].

MNPs could also self-assemble under the guidance of their intrinsic dipoles, which is a unique assembly method for them. Linear chains of superparamagnetic iron nanoparticles can be obtained without external magnetic field if the sizes of the MNPs are large enough to bring about sufficiently powerful dipole–dipole interactions [109, 110]. Furthermore, larger amount of poly(vinylpyrrolidone) (PVP) and higher reaction temperatures could transform the chain-like magnetic assemblies to nanorings [111]. The reason might be that the reaction conditions could increase the possibility of intra- and inter-chains interplay and viscosity of the solution to facilitate the formation of magnetic nanorings [112].

The moderate aggregation of MNPs can improve the magnetism, shorten the transverse relaxation time, and enhance the T_2-MRI contrast due to their larger effective size compared with dispersed MNPs [106]. The assemblies are prone to be ingested by cells in very large quantities, so they reside longer in the liver for imaging [107]. Besides, there are some gaps among nanoparticles in one cluster. Drugs could be filled into the gaps to increase the drug loading capacity [38, 108, 113]. By contrast with the isotropic assemblies, nanochains with obvious anisotropy show longer blood circulating life because they are more difficult to be engulfed by cells [29]. However, the nanochains modified by suitable ligands on their surface could provide more contact opportunities with receptors of cells and achieve better active targeting efficiency [30].

3.2.2 *External magnetic field-assisted assembly of MNPs*

Though some larger MNPs with sufficient magnetic moments can assemble spontaneously due to their dipole–dipole interactions, the external magnetic field can bring about quick, controllable, and convenient assembly even without extra chemical agents.

Static magnetic field has been widely applied to regulate the assembly of nanoparticles with good magnetic response [29, 30, 114, 115]. In the presence of the static magnetic field, magnetic moment of each nanoparticle would freely rotate to orient along the direction of the external magnetic field. The nanoparticles can form head-to-tail structures to minimize the systematic energy [114]. In particular, the rotating magnetic field composed of two magnets fixed on a motor can result in the formation of disk-like assemblies of magnetic nanoparticles [116]. The process of assembly might be attributed to the coupled interaction of magnetic dipolar force, a torsional force from the rotation field and viscous resistance from the fluid.

Apart from static magnetic fields, alternating-current magnetic fields have also been exploited to control and modulate the assembled structures [117, 118]. The Fe_3O_4 nanoparticles aggregated into mesoscale fibers with several hundreds of micrometers length under the assistance of external ACMF. The fibrous assembly of Fe_3O_4 nanoparticles might result from the competition between the surface-charge-controlled electrostatic interaction and the external-field-induced magnetic moment interaction. When the moments inside neighboring clusters were antiparallel, the attractive magnetic force between two moments brought two clusters together and further induced the formation of microfibers. Furthermore, the assembly was dependent upon the difference between colloidal relaxation time and the frequency of ACMF [119]. It is noteworthy that the above-mentioned fibrous aggregates still retained superparamagnetism, which is identical to that of individual nanoparticles.

The assembly of MNPs in hydrogel has some special properties because hydrogel can be easily integrated with some functional materials to play a synergistic role [35, 39, 116, 120, 121]. These assemblies can maintain relatively stable structures and orientation due to special mechanical properties. With the assistance of a static magnetic field or a rotating magnetic field, we fabricated novel magnetic hydrogel platforms through assembling the magnetic nanospheres in monomers solution before gelation [35, 116]. The aligned one-dimensional or disk-like assemblies were formed separately, and they exhibited not only anisotropy of mechanical property but also anisotropy of magnetism. Hence, the thermogenesis of the novel magnetic hydrogel was direction-dependent and can be regulated by altering the included angle between the assemblies and the alternating magnetic field. As shown in Figs. 6(a)–6(c), the thermogenesis was increased and the increment was greater in the direction along the chains than that in the direction normal to the chains. The slopes of heating curves of magnetic hydrogel indicated that the magnetothermal efficiency (heating rate) was inversely proportional to the included angle between the chains and the alternating magnetic field (Fig. 6(d)). In parallel, the release of pre-loaded drug from the aligned magnetic hydrogel can be controlled by altering the thermogenesis (Fig. 6(e)). In addition to the anisotropic magnetism, the magnetic field-induced colloidal assembly of MNPs on the surface of hydrogel could form cell-adhesive micropatterns. Consequently, the micropatterns would influence the behaviors of cancer cells, including adhesion, growth, and migration [120]. It has been proved that the magnetic hydrogel can facilitate the spontaneous formation of multicellular spheroids rather than the loose, irregular aggregates by hanging drop culture systems [39, 121]. Therefore, the anisotropic magnetic hydrogel is promising as a multicellular spheroids culturing platform.

External magnetic field assisted assembly was attempted to extend to other nanomaterials, such as noble metal [122, 123] and biological macromolecules [124–126]. Their magnetic-induced assembly was formed due to the intrinsic magnetism or the conjugation with magnetic materials. Horseradish peroxidase (HRP) was aggregated into the quasi-one-dimensional assembly in the presence of ACMF and its biological activity was hardly influenced by the external magnetic field [127].

3.2.3 *Interface induced assembly of MNPs*

Interfacial force could induce the aggregation of MNPs along the interface to minimize the interfacial energy [128]. During the period of assembly, the interface acts as a template [129]. According to the different positions of MNPs in the assembly, we roughly classify the assemblies into solid/liquid (gas) interface induced procedure, gas/liquid interface induced procedure, and liquid/liquid interface induced procedure.

Solid/liquid (gas) interface induced assembly mainly refers to orienting alignment of MNPs by classical templates. The most common way is through the layer-by-layer absorption of MNPs on the surface of templates to synthesize continuous layers as magnetic coatings. The templates used in the assembly can be not only inorganic substrates, such as glass [34, 130], silicon [131], and graphene (oxide) [132] but also organic substrates, such as poly-D,L-lactic acid (PLA) scaffold [133]. The number of assembly layers can be regulated easily to generate nanomaterials with different properties [131]. Besides, some nanomaterials owning specific shapes or some biomass, including carbon nanotubes [134], noble metal nanorods [135], polysaccharides [136], and virus [137] are also decent templates for the fabrication of magnetic nanoassemblies.

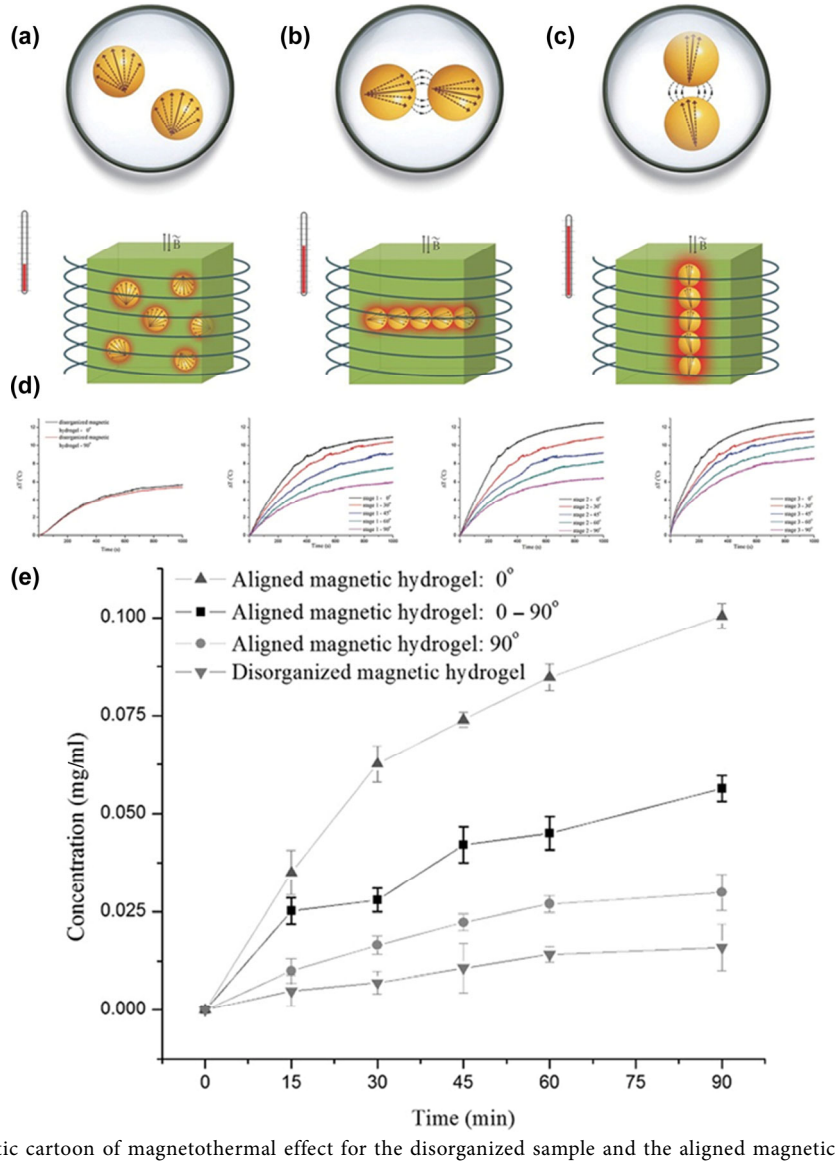

Figure 6 (a)–(c) Schematic cartoon of magnetothermal effect for the disorganized sample and the aligned magnetic sample in two directions. (d) Magnetothermal curves of disorganized magnetic hydrogel and aligned magnetic hydrogel with chains immobilized at 3, 15, and 45 min, respectively (from the left to the right). (e) *In vitro* release of pre-loaded Doxorubicin from the aligned magnetic hydrogel (with α = 0° and 90°) and the disorganized magnetic hydrogel under the alternating magnetic field. 0°–90° means the angle switching between 0° and 90°. (Adapted with permission from Ref. [35], © WILEY-VCH Verlag GmbH & Co. KGaA, Weinheim 2015).

Gas/liquid interface can also assist the assemblies of nanoparticles. The nuclei of MNPs in the liquid phase will spontaneously aggregate onto the surface of gas bubbles. Then, these nuclei grow into magnetic materials through crystallization [138, 139] or simple connection by surfactant [140, 141] to form a hollow structure later. For instance, single-crystalline Fe_3O_4 hollow spheres composed of well-aligned nanoparticles were developed using the coordination compound $[Fe(urea)_6]Cl_3$ as the sole iron source [139]. During these assemblies, the gas bubbles play an essential role just like a soft template and the MNPs lie on the interface between the gas and liquid phase.

Sometimes, the MNPs after assembly might be concentrated in the gaps between double polymer shells [36, 40, 142] or coupled to the shell surface of a microvesicle [143–145], which is induced by the liquid/liquid interface. In common cases, the surfactants are necessary to relieve surface tension to get a stable emulsion. Our group developed a series of magnetic microbubbles [41, 146] and microcontainers [142, 147] using a double-emulsion procedure to entrap MNPs into the oil layer (inner layer) of a double-layered structure (Figs. 7(a) and 7(b)). The cores of microbubbles and microcontainers are filled with gas and solution separately, which are the primary difference between them. Moreover, some researchers have attempted to combine the MNPs to the surface of microvesicles through electrostatic adsorption [145, 148] and covalent coupling [143, 144, 149]. Covalent coupling can provide stronger binding force than physical methods but it would also bring about the uneven cross-linking and agglomeration. Compared to embedding MNPs in the shells of microbubbles, coupling them on the surfaces of the microbubbles can enhance the qualities of both US and magnetic resonance (MR) imaging [143], at the expense of the elastic modulus of microbubbles [149]. Fortunately, the magnetic microvesicles can retain the same magnetism of corresponding nanoparticles regardless of surface coupling or embedding treatment.

By restricting the concentration of MNPs within a certain range, the stability of microbubbles can be increased to obtain higher scattering intensity and better contrast for US images [40, 146]. Due to the inherent magnetism of MNPs distributed in the shell, the magnetic microbubbles can be used as contrast agents for the double-modality (US and MR) imaging [41, 150]. As shown in Fig. 7(c), the enhancement efficiency of US

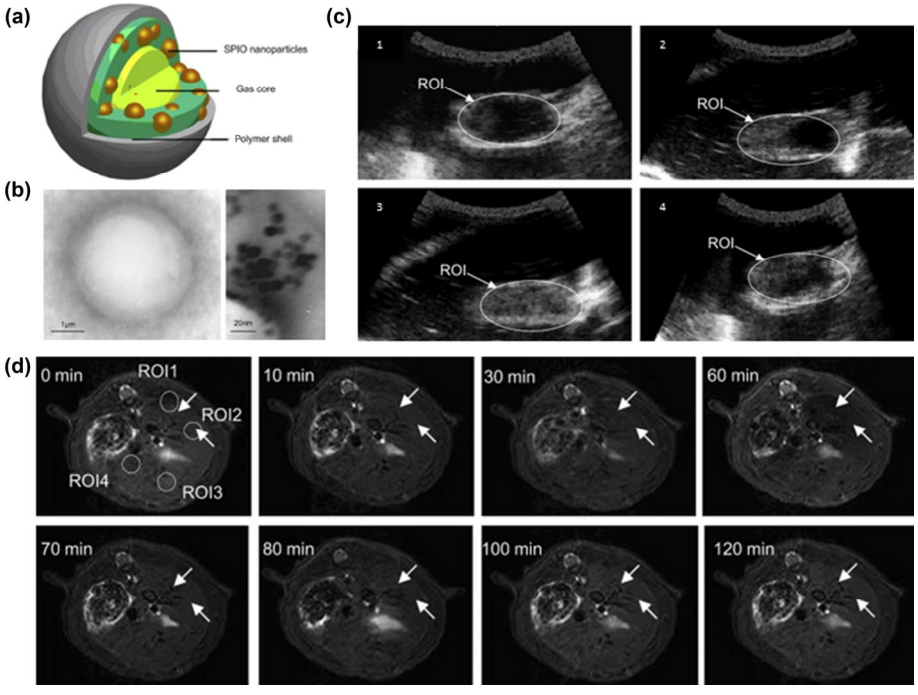

Figure 7 (a) The schematic diagram of the designed SPIO-inclusion encapsulated microbubble. (b) A transmission electron microscope (TEM) image of an SPIO-inclusion microbubble and the enlarged view of a portion of the shell. (c) The *in vitro* US imaging in the different samples: (1) de-gassed and de-ionized water; (2) non-SPIO-inclusion microbubbles; (3) 86.47 μg/mL and (4) 180.23 μg/mL SPIO concentration inclusion microbubbles. (d) Corresponding anatomical structure images from the same rat at two adjacent slice locations during SPIO-inclusion microbubble injection. The image shows that with the time lapse after injection, the T_2 signal in liver decreases at first and then increases (arrows). (Adapted with permission from Ref. [41], © Elsevier Ltd. 2009).

contrast was remarkable in the presence of SPIO-inclusion microbubbles with the appropriate insertion concentration of about 86.47 μg/mL. Meanwhile, the overall signal of MRI in the liver region was negatively enhanced after injection of the microbubble contrast agents. Apart from the refilled gas in microbubbles, the *in situ* nitric oxide (NO) gas can be generated by the L-arginine in the microcontainers under the control of external magnetic field [142, 147]. The *in situ* gas can be imaged by US or further applied for therapy as a drug [151–153]. Besides, the microbubbles and US allow the MNPs to pass through the cell membrane via a non-internalizing uptake route [154]. The efficient and low-cytotoxic cytosolic delivery strategy shows potential in nanoparticle delivery [155] and cell labeling [156].

4 Specific effects of medical MNMs

4.1 Magnetic effect

4.1.1 *Influence on nuclear magnetic resonance*

Compared with other clinical imaging tools, MRI, working on the principle of the relaxations of hydrogen nuclear spins, can provide more anatomic details, stronger soft tissue contrast, and higher spatial resolutions [157]. However, it does not always offer sufficient contrast between two tissue types with similar proton density and relaxation time. While the proton density of a tissue is fixed, the MNPs can vary the relaxation time to enhance the MRI contrast because their magnetism can alter the magnetic characteristics of nearby water protons.

There are two types of relaxation: longitudinal relaxation (T_1 relaxation) and transverse relaxation (T_2 relaxation), corresponding to T_1-weighted MRI and T_2-weighted MRI. In general, MNPs can affect both relaxation processes, but their impact on T_2 relaxation is much greater than that on T_1 relaxation to result in dark signals [1, 106, 158–161]. Size can greatly affect the magnetic properties of nanoparticles. The T_2 contrast-enhancing effect first rose and then declined with increasing size of nanoparticles, and the best result emerged when the edge length of MNPs was about 22 nm [91, 162]. This special phenomenon can be illustrated by three different regimes: motional average regime (MAR), static dephasing regime (SDR), and echo-limiting regime (ELR) [163]. The r_2 relaxivity (761 $mM^{-1}\cdot s^{-1}$) of about 22 nm MNPs was very close to the theoretically predicted maximum r_2 value (approximately 800 $mM^{-1}\cdot s^{-1}$).

T_1 contrast imaging is usually preferred for better clarity in clinical procedures because the dark signal produced by T_2 contrast agents is sometimes confused with some endogenous conditions, such as calcification, air, hemorrhage, and blood clots [2]. Many studies denoted that ultra-small SPIONPs exhibited enhanced T_1 contrast effects as positive agents, while their T_2 contrast effects were relatively weak [93, 96, 164, 165]. It mainly resulted from that the r_2 values decreased more quickly than r_1 values with reducing size to get lower r_2/r_1 ratio. The high r_1 relaxivity of 3.93 $mM^{-1}\cdot s^{-1}$ and extremely low r_2/r_1 ratio of 1.93 indicate the T_1 MRI contrast of ultra-small MIONPs can be comparable to that of Gd-based positive contrast agents [96].

In order to obtain complementary information on T_1-weighted MRI and T_2-weighted MRI, simultaneous acquisition of positive and negative contrasts has been extensively pursued [101, 166]. Commonly, dual-mode MRI can be realized through tailoring MIONPs by incorporating paramagnetic metal ions. Based on the different accumulation rates of the nanoparticles in different tissues, only ultra-small Fe_3O_4 nanoparticles can be used to achieve time-dependent T_1–T_2 switchable MRI [94, 95]. In normal liver tissues, the nanoparticles can be quickly phagocytosed by a reticuloendothelial system, and accumulate in the liver to improve the T_2-weighted effect. Nanoparticles that are not phagocytosed are delivered into the tumor tissues due to the enhanced permeation and retention (EPR) effect, and dispersed enough to act as T_1 contrast agents.

MNPs with high biocompatibility have significant potential to be an alternative MRI contrast agent in clinical tumor diagnosis to substitute for the Gd-chelates with potential toxicity of the Gd^{3+} ion [167, 168]. They can also be used in *in vivo* tracing through MRI to reveal some mechanisms about the interactions between MNPs and biological tissues [160, 169, 170].

4.1.2 *Magnetomechanical property*

A distinctive advantage of the magnetomechanical property of MNPs is their manipulability by an external magnetic field [171]. The above-mentioned assembly of MNPs induced by magnetic field (mentioned in Section 3.2.2) is a living example of using their magnetomechanical property. Moreover, MNPs can be applied in magnetic guidance both *in vitro* and *in vivo*.

Usually, the magnetic guidance is conducted by applying permanent magnets on magnetic nanocarriers. Specific biomolecules coupled with MNPs could be separated from the mixture solely based on the magnetic force originating from permanent magnets, which is called magnetic bioseparation [62, 172, 173]. Besides, in gene transfection, MNPs can be pulled toward cells with the assistance of external magnetic field, which subsequently facilitates the efficient and rapid delivery of genes or nucleic acids [174, 175]. This magnetofection could significantly enhance the level of transgene expression by hundreds of times compared to the conventional transfection systems [6, 176].

Apart from the *in vitro* application, the concept of magnetic guidance is also manifested in *in vivo* magnetic targeting. Under the guidance of an external magnetic field, therapeutics-loading MNPs [1, 171] and magnetic assemblies, such as microbubbles [4], microspheres [177], liposomes [152, 178], and aerosols [179] can be delivered more selectively to the target site with a lower systemic distribution of the cytotoxic drug. Even for some somatic and germ cells, like platelets [151], erythrocytes [180], and sperms [5], combining with magnetic materials can also be controlled by magnetic field as promising nanocarriers. Biomimetic drug carries derived from human endogenous cells have advantages of higher biosafety, targeting abilities, and somatic cell-fusion abilities than artificial carriers. Recently, our group has discovered that a focused magnetic field could direct the aggregation of magnetic erythrocytes into a specific region for quick modeling of vascular diseases [180]. Though many studies have proved the effectiveness of external magnetic field on the drug delivery, for deep tissues in body, a deeply-buried magnet might be more preferable to guide the MNPs [171].

4.1.3 *Magnetothermal effect*

MNPs could generate heat under an external ACMF, which is called the magnetothermal effect. As mentioned above, the heat generation efficiency is size-dependent, which roots from the intrinsic differences in the magnetothermal mechanisms of large and small MNPs. The optimal size of MNPs for thermogenesis might be about 20 nm corresponding to the max SAR values and specific loss power (SLP). Besides, the assembled MNPs will exhibit magnetothermal anisotropy [130, 133]. The orientation of the magnetic assembly relative to an external field can control the thermogenesis, which arises from the principle of energy conservation formulated by Poynting's theorem in electromagnetics [34]. Then, it is firstly proved that the thermogenesis of MNPs is directly related to the energy flux of the field rather than to the field's intensity.

The magnetothermal effect of MNPs has been utilized for a thermal therapy known as thermal ablation or hyperthermia, due to their noninvasive and selective nature with minimal damage to normal cells [181, 182]. Unfortunately, limited by the poor heating conversion efficiencies of MNPs under ACMF, a high dose of MNPs is generally required to achieve appropriate therapeutic effect [18]. However, the high dosage leads to high cost and non-targeted deposition. Above-mentioned efforts, such as regulating MNPs' sizes, morphologies, compositions, or aggregating as-synthesized MNPs in an orderly arrangement, have been confirmed to contribute effectively to magnetic hyperthermia therapy. Moreover, some novel drug-loaded magnetic nanocomposites have been built to realize magnetic hyperthermia and chemotherapy synergistically [183, 184]. They are stabilized with shells of biocompatible materials and can be taken up by tumor cells. As a magnetothermal responsive nanocarrier, after exposure to ACMF, the magnetic hyperthermia and supersensitive drug release to kill cancer cells simultaneously.

Though high temperature caused by MNPs in ACMF could kill tumor cells, they might also give rise to deleterious effects on surrounding normal tissues. To guarantee the curative effect and protect the surrounding normal tissues simultaneously, some strategies should be developed to estimate and control the temperatures. Infrared thermography [185] or thermoresponsive fluorescent polymers [186] were used to monitor the surface temperature of tumors. Temperature distribution of the whole tumor could be further obtained with the assistance of the thermal model or numerical simulation for an accurate and customized treatment plan [187, 188]. In practice, the combination of ACMF and static magnetic field could precisely control the heating position and area [189]. Furthermore, a magnetic nanoemulsion hydrogel could be securely restricted in tumor tissues without diffusion and leakage due to the rapid intra-tumor gelation [3]. In order to pursue more biocompatibility, injectable ferromagnetic silk fibroin hydrogel was used for magnetic hyperthermia ablation. The hydrogel was made by natural biopolymer silk fibroin, and it did not reduce the viability of cells and function of the main organs in mice [190]. These methods can reduce the side effects on the non-therapeutic area in terms of selective heating and accumulation.

4.2 Enzyme-like activity

Yan and co-workers first reported that Fe_3O_4 nanoparticles in fact possess an intrinsic enzyme mimetic activity similar to that found in natural HRP [92]. The peroxidase (POD) activity was caused by producing hydroxyl radicals (•OH) based on the Fenton reaction. Then, more MNPs were found to have similar enzyme-like activities, such as γ-Fe_2O_3 [191, 192], CeO_2 [193], Co_3O_4 [97, 194], and PBNPs [195–197], though the mechanisms of enzyme-like activities might be different. Since MNPs are inorganic materials, they are generally more stable than the proteins with enzymatic activities at extreme pH and high temperatures.

The enzyme-like activity of MNPs could be regulated through adjusting their intrinsic properties. For instance, a greater surface-to-volume ratio caused by shrinking in size of the MNPs would promote the catalytic activities between the nanoparticles and the substrates [92, 198]. Besides, the morphology of MNPs also plays an important role in catalytic activities (nanoplates > nanopolyhedrons > nanorods > nanocubes), which was determined by the exposure of crystal planes [97]. Some strategies for the modification of MNPs with other inorganic [191, 199, 200] or organic materials [201] were also developed to enhance the performance of the nanozyme. The essence of the above-mentioned regulation methods is the adjustment of catalytic sites and binding affinities.

In addition to their intrinsic property, specific circumstance can also give rise to interesting influence on the enzyme-like activity. We first found that MIONPs, including Fe_3O_4 and γ-Fe_2O_3, exhibited more catalase (CAT) activity at neutral conditions (pH = 7.4) but more POD activity in acid conditions (pH = 4.8). It meant MIONPs possessed pH-dependent dual enzyme mimetic properties [192]. At pH 4.8, both of them could catalyze the oxidation of substrate 3,3',5,5'-tetramethylbenzidine (TMB) in the presence of H_2O_2, which was accompanied by color change to blue several minutes after IONPs were added into the H_2O_2/TMB reaction system (Fig. 8(a), tubes 2–5). Additionally, the ultraviolet–visible (UV–vis) absorption–time course curves indicated that Fe_3O_4 had a higher peroxidase-like activity than Fe_2O_3 under the same conditions (Fig. 8(b)). In a neutral condition, gas bubbles were observed in tubes containing MIONPs diluted and H_2O_2 (Fig. 8(c)), which indicated that MIONPs might behave similarly as catalase to decompose H_2O_2 into water and oxygen. The results, as shown in the dissolved oxygen–time course curves of H_2O_2 (Fig. 8(d)), demonstrated Fe_3O_4 also had a higher catalase-like activity than Fe_2O_3 NPs. Consequently, the multienzyme activities, containing POD, CAT, and superoxide dismutase (SOD) activity, of Co_3O_4 [194] and PBNPs [196] at different pH values were also discovered (Fig. 9). Our group theorized for the first time that the multienzyme-like activities were likely attributed to the abundant redox potentials of their different forms, making them efficient electron transporters. Wang et al. pointed out that "whether other peroxidase mimics have dual enzyme mimicking activities should be examined in the future" in view of the above-mentioned studies [202].

The magnetic nanozymes have shown a broad spectrum of applications in immunoassay [7, 191], immunohistochemical staining [8, 9, 194], *in vivo* imaging [203], and disease therapy [204], due to their high stability and tunable activity. For examples, Co_3O_4 NPs conjugated with Avastin antibody was used to detect vascular endothelial growth factor (VEGF) overexpressed in tumor tissues through immunohistochemical staining [194]. A new strategy to obtain an excellent US and MR dual-modality imaging for H_2O_2 diagnostics was first developed, basing on the fact that PBNPs could catalyze the breakdown of H_2O_2 into oxygen molecules under the neutral condition [203]. Due to the multienzyme-like activity of MNPs, they could be used not only for the antitumor therapeutics through reactive oxygen species (ROS) selective production caused by POD activity [197, 204, 205], but also for the prevention of inflammatory and aging-related diseases through ROS scavenging capability caused by CAT- or SOD-like activity [206]. Recently, it has been proposed that MIONPs could facilitate the oxidative decomposition of lipids through the activation of lipid-regulated proteins by the produced hydroxyl radical [205]. The enzyme-like activity of MNPs provides a novel idea for their applications in the biomedical field, but their distribution and elimination *in vivo* and how they affect body functions should be further evaluated and understood.

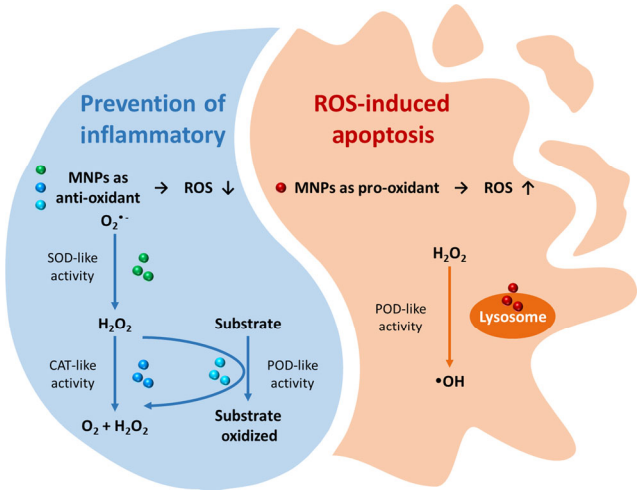

Figure 9 Bi-directional regulation of intracellular ROS by the multienzyme-like activity of MNPs in specific circumstances.

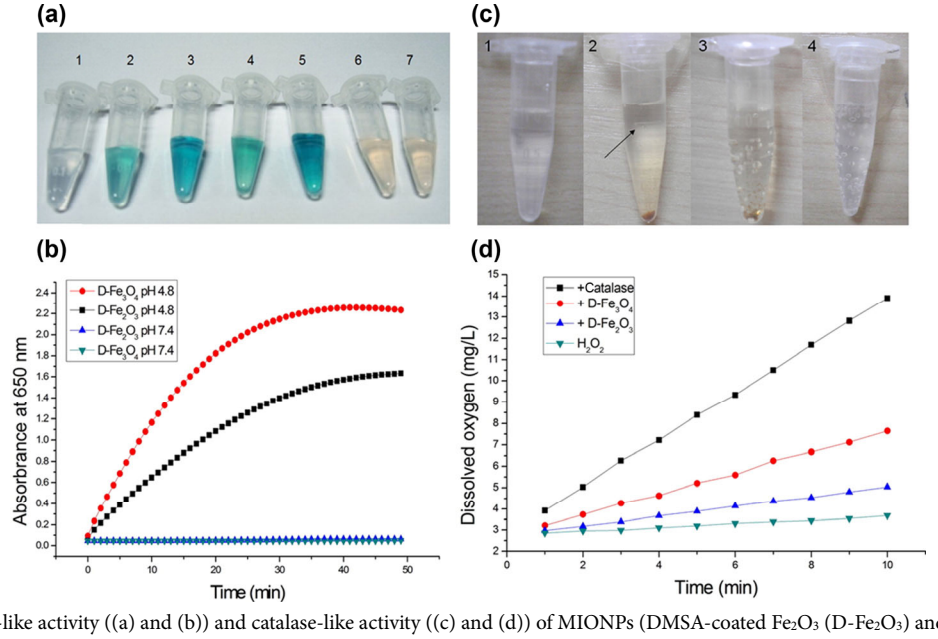

Figure 8 Peroxidase-like activity ((a) and (b)) and catalase-like activity ((c) and (d)) of MIONPs (DMSA-coated Fe_2O_3 (D-Fe_2O_3) and DMSA-coated Fe_3O_4 (D-Fe_3O_4)). (a) Photograph of color reactions after 30-min incubation. Tubes 1–5: H_2O_2 + TMB in pH 4.8 buffer plus (1) none, (2) 10 μg/mL D-Fe_2O_3, (3) 10 μg/mL D-Fe_3O_4, (4) 20 μg/mL D-Fe_2O_3, and (5) 20 μg/mL D-Fe_3O_4. Tubes 6 and 7: H_2O_2 + TMB in pH 7.4 buffer plus (6) 20 μg/mL D-Fe_2O_3 and (7) 20 μg/mL D-Fe_3O_4. (b) UV–vis absorption–time course curves of the TMB/H_2O_2 reaction system catalyzed by 20 μg/mL D-Fe_2O_3 or D-Fe_3O_4 NPs in pH 4.8 or 7.4 buffer. (c) Photograph of bubble reactions after 6-h incubation. Tubes 1–4: 100 mM H_2O_2 in pH 7.4 phosphate buffer saline (PBS) buffer plus (1) none, (2) 20 μg/mL D-Fe_2O_3 (arrow indicating very small bubbles), (3) 20 μg/mL D-Fe_3O_4, and (4) 20 U/mL catalase. (d) Dissolved oxygen–time course curves of H_2O_2 in pH 7.4 buffer catalyzed by 20 μg/mL D-Fe_2O_3 or D-Fe_3O_4 NPs or 20 U/mL catalase. (Adapted with permission from Ref. [192], © American Chemical Society 2012).

5 Conclusions and perspectives

Over the past decades, MNMs and their applications in the biological and medical filed have attracted much attention from research groups around the world. In pace with the remarkable achievements made in MNMs, various synthetic routes and effective performance regulation approaches have been widely proposed. In particular, their unique magnetism allows to couple multi physical fields in one system through applying different types of external magnetic fields. The special properties of MNPs also facilitate the improvement of the preparation methods, controlled aggregation, and biomedical applications from *in vitro* to *in vivo*. However, the development of MNMs is still full of challenges to be addressed.

(1) High-quality MNPs meeting the pharmaceutical quality criteria. At present, high-performance MNPs are usually prepared at high temperature in the organic phase. The obtained MNPs are usually toxic and hydrophobic, which cannot meet the clinical demands evidently. Thus, it is urgent to concentrate on the clinically approved MNPs, and then improve their synthetic pathways without introducing additional organic reagents to enhance the crystallinity and magnetic properties of MNPs.

(2) Understanding of the synthetic mechanisms of MNPs in detail. An in-depth understanding of the synthetic mechanisms will facilitate to separate the coexisting nucleation and growth processes, which are considered as the main factor leading to the poor performance of MNPs. Though some iron oxide nucleation and growth mechanisms have been proposed based on experimental and theoretical studies, they have not yet been universally recognized due to the influence of the complex processes, including aggregation, proton transfer, and conformational transformation. The search for the reasonable and complete mechanisms will remain an active research field.

(3) The combination between artificial intelligence technology and materials science. The artificial intelligence technology has exhibited a huge advantage in one-dimensional or two-dimensional signal processing. However, so far, most researchers still extract and integrate information from the characterization results of MNPs through manual operation. They spend a lot of time on repetitive work, but the obtained data cannot be guaranteed in terms of quality and quantity. The combination between artificial intelligence technology and materials science will bring about rapid, efficient, and automated analysis of material characteristics, and even further predict material performance based on a large amount of existing data.

The above issues to be solved will be the next frontier to further promote the rapid development of MNMs in basic research and practical applications. We believe that in the future, MNMs will have broader prospects from *in vitro* detection and incubation to *in vivo* diagnosis and treatment.

Acknowledgements

This work was supported by the National Key Research and Development Program of China (No. 2017YFA0104302) and the National Natural Science Foundation of China (Nos. 51832001, 61821002, and 31800843). We would like to express our gratitude to Zhuxiao Gu, Xiaoyang Zhu, Yu Mao, Baocai Ma, Yuan An, Bo Chen, and Zhiguo Qin for their help.

Reference

[1] Chen, L.; Wu, Y.; Wu, H. N.; Li, J. Z.; Xie, J.; Zang, F. C.; Ma, M.; Gu, N.; Zhang, Y. Magnetic targeting combined with active targeting of dual-ligand iron oxide nanoprobes to promote the penetration depth in tumors for effective magnetic resonance imaging and hyperthermia. *Acta Biomater*. **2019**, *96*, 491–504.

[2] Ahmed, H. U.; Kirkham, A.; Arya, M.; Illing, R.; Freeman, A.; Allen, C.; Emberton, M. Is it time to consider a role for MRI before prostate biopsy? *Nat. Rev. Clin. Oncol*. **2009**, *6*, 197–206.

[3] Wu, H. N.; Song, L. N.; Chen, L.; Huang, Y. X.; Wu, Y.; Zang, F. C.; An, Y. L.; Lyu, H.; Ma, M.; Chen, J. et al. Injectable thermosensitive magnetic nanoemulsion hydrogel for multimodal-imaging-guided accurate thermoablative cancer therapy. *Nanoscale* **2017**, *9*, 16175–16182.

[4] Duan, L.; Yang, F.; He, W.; Song, L. N.; Qiu, F.; Xu, N.; Xu, L.; Zhang, Y.; Hua, Z. C.; Gu, N. A multi-gradient targeting drug delivery system based on RGD-$_L$-TRAIL-labeled magnetic microbubbles for cancer theranostics. *Adv. Funct. Mater*. **2016**, *26*, 8313–8324.

[5] Xu, H. F.; Medina-Sánchez, M.; Magdanz, V.; Schwarz, L.; Hebenstreit, F.; Schmidt, O. G. Sperm-hybrid micromotor for targeted drug delivery. *ACS Nano* **2018**, *12*, 327–337.

[6] Fouriki, A.; Dobson, J. Nanomagnetic gene transfection for non-viral gene delivery in NIH 3T3 mouse embryonic fibroblasts. *Materials* **2013**, *6*, 255–264.

[7] Wei, H.; Wang, E. K. Fe_3O_4 Magnetic nanoparticles as peroxidase mimetics and their applications in H_2O_2 and glucose detection. *Anal. Chem*. **2008**, *80*, 2250–2254.

[8] Zhuang, J.; Fan, K. L.; Gao, L. Z.; Lu, D.; Feng, J.; Yang, D. L.; Gu, N.; Zhang, Y.; Liang, M. M.; Yan, X. Y. *Ex vivo* detection of iron oxide magnetic nanoparticles in mice using their intrinsic peroxidase-mimicking activity. *Mol. Pharmaceutics* **2012**, *9*, 1983–1989.

[9] Wu, Y. H.; Song, M. J.; Xin, Z.; Zhang, X. Q.; Zhang, Y.; Wang, C. Y.; Li, S. Y.; Gu, N. Ultra-small particles of iron oxide as peroxidase for immunohistochemical detection. *Nanotechnology* **2011**, *22*, 225703.

[10] Wang, P.; Ma, S. Y.; Ning, G. F.; Chen, W.; Wang, B.; Ye, D. W.; Chen, B.; Yang, Y. Z.; Jiang, Q.; Gu, N. et al. Entry-prohibited effect of kHz pulsed magnetic field upon interaction between SPIO nanoparticles and mesenchymal stem cells. *IEEE Trans. Biomed. Eng*. **2020**, *67*, 1152–1158.

[11] Meng, J.; Xiao, B.; Zhang, Y.; Liu, J.; Xue, H. D.; Lei, J.; Kong, H.; Huang, Y. G.; Jin, Z. Y.; Gu, N. et al. Super-paramagnetic responsive nanofibrous scaffolds under static magnetic field enhance osteogenesis for bone repair *in vivo*. *Sci. Rep*. **2013**, *3*, 2655.

[12] Xia, Y.; Chen, H. M.; Zhao, Y. T.; Zhang, F. M.; Li, X. D.; Wang, L.; Weir, M. D.; Ma, J. Q.; Reynolds, M. A.; Gu, N. et al. Novel magnetic calcium phosphate-stem cell construct with magnetic field enhances osteogenic differentiation and bone tissue engineering. *Mater. Sci. Eng.: C* **2019**, *98*, 30–41.

[13] Chen, H. M.; Sun, J. F.; Wang, Z. B.; Zhou, Y.; Lou, Z. C.; Chen, B.; Wang, P.; Guo, Z. R.; Tang, H.; Ma, J. Q.; et al. Magnetic cell–scaffold interface constructed by superparamagnetic IONP enhanced osteogenesis of adipose-derived stem cells. *ACS Appl. Mater. Interfaces* **2018**, *10*, 44279–44289.

[14] Liu, X. L.; Chen, S. Z.; Zhang, H.; Zhou, J.; Fan, H. M.; Liang, X. J. Magnetic nanomaterials for advanced regenerative medicine: The promise and challenges. *Adv. Mater*. **2019**, *31*, 1804922.

[15] Lu, Q. B.; Sun, J. F.; Yang, Q. Y.; Cai, W. W.; Xia, M. Q.; Wu, F. F.; Gu, N.; Zhang, Z. J. Magnetic brain stimulation using iron oxide nanoparticle-mediated selective treatment of the left prelimbic cortex as a novel strategy to rapidly improve depressive-like symptoms in mice. *Zool. Res*. **2020**, *41*, 381.

[16] Underwood, E. J. 2 - Iron. In *Trace Elements in Human and Animal Nutrition* (*Fourth Edition*). Underwood, E. J., Ed.; Academic Press: Pittsburgh, 1977; pp 13–55.

[17] Rosner, M. H.; Auerbach, M. Ferumoxytol for the treatment of iron deficiency. *Exp. Rev. Hematol*. **2011**, *4*, 399–406.

[18] Kumar, C. S. S. R.; Mohammad, F. Magnetic nanomaterials for hyperthermia-based therapy and controlled drug delivery. *Adv. Drug Delv. Rev*. **2011**, *63*, 789–808.

[19] Soo Choi, H.; Liu, W. H.; Misra, P.; Tanaka, E.; Zimmer, J. P.; Itty Ipe, B.; Bawendi, M. G.; Frangioni, J. V. Renal clearance of quantum dots. *Nat. Biotechnol*. **2007**, *25*, 1165–1170.

[20] Liu, G.; Gao, J. H.; Ai, H.; Chen, X. Y. Applications and potential toxicity of magnetic iron oxide nanoparticles. *Small* **2013**, *9*, 1533–1545.

[21] Zhang, S.; Chen, X. J.; Gu, C. R.; Zhang, Y.; Xu, J. D.; Bian, Z. P.; Yang, D.; Gu, N. The effect of iron oxide magnetic nanoparticles on smooth muscle cells. *Nanoscale Res. Lett.* **2009**, *4*, 70–77.

[22] He, S. Y.; Feng, Y. Z.; Gu, N.; Zhang, Y.; Lin, X. G. The effect of γ-Fe_2O_3 nanoparticles on *Escherichia coli* genome. *Environ. Pollut.* **2011**, *159*, 3468–3473.

[23] Ge, G. Y.; Wu, H. F.; Xiong, F.; Zhang, Y.; Guo, Z. R.; Bian, Z. P.; Xu, J. D.; Gu, C. R.; Gu, N.; Chen, X. J. et al. The cytotoxicity evaluation of magnetic iron oxide nanoparticles on human aortic endothelial cells. *Nanoscale Res. Lett.* **2013**, *8*, 215.

[24] Wu, L. H.; Mendoza-Garcia, A.; Li, Q.; Sun, S. H. Organic phase syntheses of magnetic nanoparticles and their applications. *Chem. Rev.* **2016**, *116*, 10473–10512.

[25] Wang, Y. X. Superparamagnetic iron oxide based MRI contrast agents: Current status of clinical application. *Quant. Imaging Med. Surg.* **2011**, *1*, 35–40.

[26] Chen, B.; Sun, J. F.; Fan, F. G.; Zhang, X. Z.; Qin, Z. G.; Wang, P.; Li, Y.; Zhang, X. Q.; Liu, F.; Liu, Y. L. et al. Ferumoxytol of ultrahigh magnetization produced by hydrocooling and magnetically internal heating co-precipitation. *Nanoscale* **2018**, *10*, 7369–7376.

[27] Zhu, X. Y.; Zhang, Z. H.; Mao, Y.; Li, Y.; Huang, X.; Gu, N. Applying deep learning in automatic and rapid measurement of lattice spacings in HRTEM images. *Sci. China Mater.* **2020**, *63*, 2365–2370.

[28] McKenna, K. P.; Hofer, F.; Gilks, D.; Lazarov, V. K.; Chen, C. L.; Wang, Z. C.; Ikuhara, Y. Atomic-scale structure and properties of highly stable antiphase boundary defects in Fe_3O_4. *Nat. Commun.* **2014**, *5*, 5740.

[29] Xiong, F.; Tian, J. L.; Hu, K.; Zheng, X. W.; Sun, J. F.; Yan, C. Y.; Yao, J.; Song, L. N.; Zhang, Y.; Gu, N. Superparamagnetic anisotropic nano-assemblies with longer blood circulation *in vivo*: A highly efficient drug delivery carrier for leukemia therapy. *Nanoscale* **2016**, *8*, 17085–17089.

[30] Sun, Y. X.; Yan, C. Y.; Xie, J.; Yan, D.; Hu, K.; Huang, S. X.; Liu, J. P.; Zhang, Y.; Gu, N.; Xiong, F. High-performance worm-like Mn–Zn ferrite theranostic nanoagents and the application on tumor theranostics. *ACS Appl. Mater. Interfaces* **2019**, *11*, 29536–29548.

[31] Ma, M.; Wu, Y.; Zhou, J.; Sun, Y. K.; Zhang, Y.; Gu, N. Size dependence of specific power absorption of Fe_3O_4 particles in AC magnetic field. *J. Magn. Magn. Mater.* **2004**, *268*, 33–39.

[32] Xie, J.; Yan, C. Z.; Zhang, Y.; Gu, N. Shape evolution of "Multibranched" Mn–Zn ferrite nanostructures with high performance: A transformation of nanocrystals into nanoclusters. *Chem. Mater.* **2013**, *25*, 3702–3709.

[33] Xie, J.; Yan, C. Y.; Yan, Y.; Chen, L.; Song, L. N.; Zang, F. C.; An, Y. L.; Teng, G. J.; Gu, N.; Zhang, Y. Multi-modal Mn–Zn ferrite nanocrystals for magnetically-induced cancer targeted hyperthermia: A comparison of passive and active targeting effects. *Nanoscale* **2016**, *8*, 16902–16915.

[34] Sun, J. F.; Fan, F. G.; Wang, P.; Ma, S. Y.; Song, L. N.; Gu, N. Orientation-dependent thermogenesis of assembled magnetic nanoparticles in the presence of an alternating magnetic field. *Chemphyschem* **2016**, *17*, 3377–3384.

[35] Hu, K.; Sun, J. F.; Guo, Z. B.; Wang, P.; Chen, Q.; Ma, M.; Gu, N. A novel magnetic hydrogel with aligned magnetic colloidal assemblies showing controllable enhancement of magnetothermal effect in the presence of alternating magnetic field. *Adv. Mater.* **2015**, *27*, 2507–2514.

[36] Yang, F.; Gu, A. Y.; Chen, Z. P.; Gu, N.; Ji, M. Multiple emulsion microbubbles for ultrasound imaging. *Mater. Lett.* **2008**, *62*, 121–124.

[37] Ge, J. P.; Hu, Y. X.; Yin, Y. D. Highly tunable Superparamagnetic colloidal photonic crystals. *Angew. Chem., Int. Ed.* **2007**, *46*, 7428–7431.

[38] Xiong, F.; Chen, Y. J.; Chen, J. X.; Yang, B. Y.; Zhang, Y.; Gao, H. L.; Hua, Z. C.; Gu, N. Rubik-like magnetic nanoassemblies as an efficient drug multifunctional carrier for cancer theranostics. *J. Controlled Release* **2013**, *172*, 993–1001.

[39] Tang, S. J.; Hu, K.; Sun, J. F.; Li, Y.; Guo, Z. B.; Liu, M.; Liu, Q.; Zhang, F. M.; Gu, N. High quality multicellular tumor spheroid induction platform based on anisotropic magnetic hydrogel. *ACS Appl. Mater. Interfaces* **2017**, *9*, 10446–10452.

[40] Yang, F.; Li, L.; Li, Y. X.; Chen, Z. P.; Wu, J. R.; Gu, N. Superparamagnetic nanoparticle-inclusion microbubbles for ultrasound contrast agents. *Phys. Med. Biol.* **2008**, *53*, 6129–6141.

[41] Yang, F.; Li, Y. X.; Chen, Z. P.; Zhang, Y.; Wu, J. R.; Gu, N. Superparamagnetic iron oxide nanoparticle-embedded encapsulated microbubbles as dual contrast agents of magnetic resonance and ultrasound imaging. *Biomaterials* **2009**, *30*, 3882–3890.

[42] Li, Z.; Tan, B. E.; Allix, M.; Cooper, A. I.; Rosseinsky, M. J. Direct Coprecipitation route to Monodisperse dual-functionalized magnetic iron oxide Nanocrystals without size selection. *Small* **2008**, *4*, 231–239.

[43] Sun, Y. K.; Ma, M.; Zhang, Y.; Gu, N. Synthesis of nanometer-size maghemite particles from magnetite. *Colloids Surf. A: Physicochem. Eng. Aspects* **2004**, *245*, 15–19.

[44] Chen, Z. P.; Xu, A. Q.; Zhang, Y.; Gu, N. Preparation of NiO and CoO nanoparticles using M^{2+}-oleate (M=Ni, Co) as precursor. *Curr. Appl. Phys.* **2010**, *10*, 967–970.

[45] Song, M. J.; Zhang, Y.; Hu, S. L.; Song, L.; Dong, J. L.; Chen, Z. P.; Gu, N. Influence of morphology and surface exchange reaction on magnetic properties of monodisperse magnetite nanoparticles. *Colloids Surf. A: Physicochem. Eng. Aspects* **2012**, *408*, 114–121.

[46] Seitz, T.; Thoma, R.; Schoch, G. A.; Stihle, M.; Benz, J.; D'Arcy, B.; Wiget, A.; Ruf, A.; Hennig, M.; Sterner, R. Enhancing the stability and solubility of the glucocorticoid receptor ligand-binding domain by high-throughput library screening. *J. Mol. Biol.* **2010**, *403*, 562–577.

[47] Masthoff, I. C.; Kraken, M.; Menzel, D.; Litterst, F. J.; Garnweitner, G. Study of the growth of hydrophilic iron oxide nanoparticles obtained via the non-aqueous sol–gel method. *J. Sol-Gel Sci. Technol.* **2016**, *77*, 553–564.

[48] Wan, J. Q.; Cai, W.; Meng, X. X.; Liu, E. Z. Monodisperse water-soluble magnetite nanoparticles prepared by polyol process for high-performance magnetic resonance imaging. *Chem. Commun.* **2007**, 5004–5006.

[49] Ali, R.; Khan, M. A.; Mahmood, A.; Chughtai, A. H.; Sultan, A.; Shahid, M.; Ishaq, M.; Warsi, M. F. Structural, magnetic and dielectric behavior of $Mg_{1-x}Ca_xNiyFe_{2-y}O_4$ nano-ferrites synthesized by the micro-emulsion method. *Ceram. Int.* **2014**, *40*, 3841–3846.

[50] Lu, A. H.; Salabas, E. L.; Schüth, F. Magnetic nanoparticles: Synthesis, protection, functionalization, and application. *Angew. Chem., Int. Ed.* **2007**, *46*, 1222–1244.

[51] Massart, R. Preparation of aqueous magnetic liquids in alkaline and acidic media. *IEEE Trans. Magn.* **1981**, *17*, 1247–1248.

[52] Bee, A.; Massart, R.; Neveu, S. Synthesis of very fine maghemite particles. *J. Magn. Magn. Mater.* **1995**, *149*, 6–9.

[53] Abou Hassan, A.; Sandre, O.; Cabuil, V.; Tabeling, P. Synthesis of iron oxide nanoparticles in a microfluidic device: Preliminary results in a coaxial flow millichannel. *Chem. Commun.* **2008**, 1783–1785.

[54] Kumar, K.; Nightingale, A. M.; Krishnadasan, S. H.; Kamaly, N.; Wylenzinska-Arridge, M.; Zeissler, K.; Branford, W. R.; Ware, E.; deMello, A. J.; deMello, J. C. Direct synthesis of dextran-coated superparamagnetic iron oxide nanoparticles in a capillary-based droplet reactor. *J. Mater. Chem.* **2012**, *22*, 4704–4708.

[55] Chen, B.; Li, Y.; Zhang, X. Q.; Liu, F.; Liu, Y. L.; Ji, M.; Xiong, F.; Gu, N. An efficient synthesis of ferumoxytol induced by alternating-current magnetic field. *Mater. Lett.* **2016**, *170*, 93–96.

[56] Li, Y.; Hu, K.; Chen, B.; Liang, Y. J.; Fan, F. G.; Sun, J. F.; Zhang, Y.; Gu, N. Fe_3O_4@PSC nanoparticle clusters with enhanced magnetic properties prepared by alternating-current magnetic field assisted co-precipitation. *Colloids Surf. A: Physicochem. Eng. Aspects* **2017**, *520*, 348–354.

[57] Qin, Z. G.; Chen, B.; Huang, X.; Mao, Y.; Li, Y.; Yang, F.; Gu, N. Magnetic internal heating-induced high performance Prussian blue nanoparticle preparation and excellent catalytic activity. *Dalton Trans.* **2019**, *48*, 17169–17173.

[58] Liang, Y. J.; Zhang, Y.; Guo, Z. R.; Xie, J.; Bai, T. T.; Zou, J. M.; Gu, N. Ultrafast preparation of Monodisperse Fe_3O_4 nanoparticles by microwave-assisted thermal decomposition. *Chem.—Eur. J.* **2016**, *22*, 11807–11815.

[59] Liang, Y. J.; Fan, F. G.; Ma, M.; Sun, J. F.; Chen, J.; Zhang, Y.; Gu, N. Size-dependent electromagnetic properties and the related simulations of Fe_3O_4 nanoparticles made by microwave-assisted

thermal decomposition. *Colloids Surf. A*: *Physicochem. Eng. Aspects* **2017**, *530*, 191–199.
[60] Erdemir, D.; Lee, A. Y.; Myerson, A. S. Nucleation of crystals from solution: Classical and two-step models. *Acc. Chem. Res.* **2009**, *42*, 621–629.
[61] Wang, F. D.; Richards, V. N.; Shields, S. P.; Buhro, W. E. Kinetics and mechanisms of aggregative Nanocrystal growth. *Chem. Mater.* **2014**, *26*, 5–21.
[62] Sun, J. F.; Xu, R.; Zhang, Y.; Ma, M.; Gu, N. Magnetic nanoparticles separation based on nanostructures. *J. Magn. Magn. Mater.* **2007**, *312*, 354–358.
[63] Sun, J. F.; He, M. M.; Liu, X.; Gu, N. Optimizing colloidal dispersity of magnetic nanoparticles based on magnetic separation with magnetic nanowires array. *Appl. Phys. A* **2015**, *118*, 569–577.
[64] Jordan, A.; Maier-Hauff, K. Magnetic nanoparticles for intracranial thermotherapy. *J. Nanosci. Nanotechnol.* **2007**, *7*, 4604–4606.
[65] de Haan, K.; Ballard, Z. S.; Rivenson, Y.; Wu, Y. C.; Ozcan, A. Resolution enhancement in scanning electron microscopy using deep learning. *Sci. Rep.* **2019**, *9*, 12050.
[66] Qiao, C.; Li, D.; Guo, Y. T.; Liu, C.; Jiang, T.; Dai, Q. H.; Li, D. Evaluation and development of deep neural networks for image super-resolution in optical microscopy. *Nat. Methods* **2021**, *18*, 194–202.
[67] Odziomek, K.; Ushizima, D.; Oberbek, P.; Kurzydłowski, K. J.; Puzyn, T.; Haranczyk, M. Scanning electron microscopy image representativeness: Morphological data on nanoparticles. *J. Microsc.* **2017**, *265*, 34–50.
[68] Sun, B. C.; Barnard, A. S. Texture based image classification for nanoparticle surface characterisation and machine learning. *J. Phys.: Mater.* **2018**, *1*, 016001.
[69] Han, B. N.; Lin, Y. X.; Yang, Y. F.; Mao, N. N.; Li, W. Y.; Wang, H. Z.; Yasuda, K.; Wang, X. R.; Fatemi, V.; Zhou, L.; et al. Deep-learning-enabled fast optical identification and characterization of 2D materials. *Adv. Mater.* **2020**, *32*, 2000953.
[70] Güven, G.; Oktay, A. B. Nanoparticle detection from TEM images with deep learning. In *Proceedings of the 2018 26th Signal Processing and Communications Applications Conference* (*SIU*), Izmir, Turkey, 2018; pp 1–4.
[71] Roberts, G.; Haile, S. Y.; Sainju, R.; Edwards, D. J.; Hutchinson, B.; Zhu, Y. Y. Deep learning for semantic segmentation of defects in advanced STEM images of steels. *Sci. Rep.* **2019**, *9*, 12744.
[72] Lee, B.; Yoon, S.; Lee, J. W.; Kim, Y.; Chang, J.; Yun, J.; Ro, J. C.; Lee, J. S.; Lee, J. H. Statistical characterization of the morphologies of nanoparticles through machine learning based electron microscopy image analysis. *ACS Nano* **2020**, *14*, 17125–17133.
[73] Ahn, T.; Kim, J. H.; Yang, H. M.; Lee, J. W.; Kim, J. D. Formation pathways of magnetite nanoparticles by Coprecipitation method. *J. Phys. Chem. C* **2012**, *116*, 6069–6076.
[74] Liu, H. Y.; Sun, J. F.; Wang, H. Y.; Wang, P.; Song, L. N.; Li, Y.; Chen, B.; Zhang, Y.; Gu, N. Quantitative evaluation of the total magnetic moments of colloidal magnetic nanoparticles: A kinetics-based method. *ChemPhysChem* **2015**, *16*, 1598–1602.
[75] Wang, H. Y.; Ge, Y. Q.; Sun, J. F.; Wang, H.; Gu, N. Magnetic sensor based on image processing for dynamically tracking magnetic moment of single magnetic mesenchymal stem cell. *Biosens. Bioelectron.* **2020**, *169*, 112593.
[76] Alexandrov, V.; Rosso, K. M. *Ab initio* modeling of Fe(II) adsorption and interfacial electron transfer at goethite (α-FeOOH) surfaces. *Phys. Chem. Chem. Phys.* **2015**, *17*, 14518–14531.
[77] Kerisit, S.; Zarzycki, P.; Rosso, K. M. Computational molecular simulation of the oxidative adsorption of ferrous iron at the hematite (001)–water interface. *J. Phys. Chem. C* **2015**, *119*, 9242–9252.
[78] Jones, F.; Rohl, A. L.; Farrow, J. B.; van Bronswijk, W. Molecular modeling of water adsorption on hematite. *Phys. Chem. Chem. Phys.* **2000**, *2*, 3209–3216.
[79] Zhang, H. Z.; Waychunas, G. A.; Banfield, J. F. Molecular dynamics simulation study of the early stages of nucleation of iron Oxyhydroxide nanoparticles in aqueous solutions. *J. Phys. Chem. B* **2015**, *119*, 10630–10642.
[80] Kawska, A.; Duchstein, P.; Hochrein, O.; Zahn, D. Atomistic mechanisms of ZnO Aggregation from Ethanolic solution: Ion association, proton transfer, and self-organization. *Nano Lett.* **2008**, *8*, 2336–2340.
[81] Debus, C.; Wu, B. H.; Kollmann, T.; Duchstein, P.; Siglreitmeier, M.; Herrera, S.; Benke, D.; Kisailus, D.; Schwahn, D.; Pipich, V. et al. Bioinspired multifunctional layered magnetic hybrid materials. *Bioinsp., Biomim. Nanobiomater.* **2019**, *8*, 28–46.
[82] Siglreitmeier, M.; Wu, B. H.; Kollmann, T.; Neubauer, M.; Nagy, G.; Schwahn, D.; Pipich, V.; Faivre, D.; Zahn, D.; Fery, A. et al. Multifunctional layered magnetic composites. *Beilstein J. Nanotechnol.* **2015**, *6*, 134–148.
[83] Baumgartner, J.; Dey, A.; Bomans, P. H. H.; Le Coadou, C.; Fratzl, P.; Sommerdijk, N. A. J. M.; Faivre, D. Nucleation and growth of magnetite from solution. *Nat. Mater.* **2013**, *12*, 310–314.
[84] Zhang, J.; Lei, Y. K.; Zhang, Z.; Chang, J. H.; Li, M. D.; Han, X.; Yang, L. J.; Yang, Y. I.; Gao, Y. Q. A perspective on deep learning for molecular modeling and simulations. *J. Phys. Chem. A* **2020**, *124*, 6745–6763.
[85] Zhang, L. F.; Han, J. Q.; Wang, H.; Car, R.; E, W. Deep potential molecular dynamics: A scalable model with the accuracy of quantum mechanics. *Phys. Rev. Lett.* **2018**, *120*, 143001.
[86] Yan, T.; Sun, B. C.; Barnard, A. S. Predicting archetypal nanoparticle shapes using a combination of thermodynamic theory and machine learning. *Nanoscale* **2018**, *10*, 21818–21826.
[87] Zhang, J. W.; Chen, J. F.; Hu, P. J.; Wang, H. F. Identifying the composition and atomic distribution of Pt-Au bimetallic nanoparticle with machine learning and genetic algorithm. *Chin. Chem. Lett.* **2020**, *31*, 890–896.
[88] Sun, B. C.; Fernandez, M.; Barnard, A. S. Machine learning for silver nanoparticle electron transfer property prediction. *J. Chem. Inf. Model.* **2017**, *57*, 2413–2423.
[89] Jang, J. T.; Nah, H.; Lee, J. H.; Moon, S. H.; Kim, M. G.; Cheon, J. Critical enhancements of MRI Contrast and Hyperthermic effects by dopant-controlled magnetic nanoparticles. *Angew. Chem., Int. Ed.* **2009**, *48*, 1234–1238.
[90] Wang, C. Y.; Hong, J. M.; Chen, G.; Zhang, Y.; Gu, N. Facile method to synthesize oleic acid-capped magnetite nanoparticles. *Chin. Chem. Lett.* **2010**, *21*, 179–182.
[91] Chen, L.; Xie, J.; Wu, H. A.; Li, J. Z.; Wang, Z. M.; Song, L. N.; Zang, F. C.; Ma, M.; Gu, N.; Zhang, Y. Precise study on size-dependent properties of magnetic iron oxide nanoparticles for *in vivo* magnetic resonance imaging. *J. Nanomater.* **2018**, *2018*, 3743164.
[92] Gao, L. Z.; Zhuang, J.; Nie, L.; Zhang, J. B.; Zhang, Y.; Gu, N.; Wang, T. H.; Feng, J.; Yang, D. L.; Perrett, S.; et al. Intrinsic peroxidase-like activity of ferromagnetic nanoparticles. *Nat. Nanotechnol.* **2007**, *2*, 577–583.
[93] Jia, Z. Y.; Song, L. N.; Zang, F. C.; Song, J. C.; Zhang, W.; Yan, C. Z.; Xie, J.; Ma, Z. L.; Ma, M.; Teng, G. J. et al. Active-target T_1-weighted MR imaging of tiny hepatic tumor via RGD modified ultra-small Fe_3O_4 nanoprobes. *Theranostics* **2016**, *6*, 1780–1791.
[94] Bai, C.; Jia, Z. Y.; Song, L. N.; Zhang, W.; Chen, Y.; Zang, F. C.; Ma, M.; Gu, N.; Zhang, Y. Time-dependent T_1–T_2 switchable magnetic resonance imaging realized by c(RGDyK) modified Ultrasmall Fe_3O_4 Nanoprobes. *Adv Funct. Mater* **2018**, *28*, 1802281.
[95] Bai, C.; Hu, P. C.; Liu, N. L.; Feng, G. D.; Liu, D.; Chen, Y.; Ma, M.; Gu, N.; Zhang, Y. Synthesis of Ultrasmall Fe_3O_4 nanoparticles as T_1–T_2 dual-modal magnetic resonance imaging contrast agents in rabbit hepatic tumors. *ACS Appl. Nano Mater.* **2020**, *3*, 3585–3595.
[96] Chen, B.; Guo, Z. H.; Guo, C. X.; Mao, Y.; Qin, Z. G.; Ye, D. W.; Zang, F. C.; Lou, Z. C.; Zhang, Z. H.; Li, M. Y. et al. Moderate cooling coprecipitation for extremely small iron oxide as a pH dependent T_1-MRI contrast agent. *Nanoscale* **2020**, *12*, 5521–5532.
[97] Zhang, W.; Dong, J. L.; Wu, Y.; Cao, P.; Song, L.; Ma, M.; Gu, N.; Zhang, Y. Shape-dependent enzyme-like activity of Co_3O_4 nanoparticles and their conjugation with his-tagged EGFR single-domain antibody. *Colloids Surf. B*: *Biointerf.* **2017**, *154*, 55–62.
[98] Ma, M.; Zhang, Y.; Guo, Z. R.; Gu, N. Facile synthesis of ultrathin magnetic iron oxide nanoplates by Schikorr reaction. *Nanoscale Res. Lett.* **2013**, *8*, 16.
[99] Zhou, Z. J.; Wang, L. R.; Chi, X. Q.; Bao, J. F.; Yang, L. J.; Zhao, W. X.; Chen, Z.; Wang, X. M.; Chen, X. Y.; Gao, J. H. Engineered iron-oxide-based nanoparticles as enhanced T_1 contrast agents for efficient tumor imaging. *ACS Nano* **2013**, *7*, 3287–3296.
[100] Park, J. Y.; Baek, M. J.; Choi, E. S.; Woo, S.; Kim, J. H.; Kim, T. J.; Jung, J. C.; Chae, K. S.; Chang, Y.; Lee, G. H. Paramagnetic

Ultrasmall gadolinium oxide nanoparticles as advanced T_1 MRI contrast agent: Account for large longitudinal Relaxivity, optimal particle diameter, and *in vivo* T_1 MR images. *ACS Nano* **2009**, *3*, 3663–3669.

[101] Shin, T. H.; Choi, J. s.; Yun, S.; Kim, I. S.; Song, H. T.; Kim, Y.; Park, K. I.; Cheon, J. T_1 and T_2 dual-mode MRI contrast agent for enhancing accuracy by engineered Nanomaterials. *ACS Nano* **2014**, *8*, 3393–3401.

[102] Walz, F. The Verwey transition—a topical review. *J. Phys.: Condens. Matter* **2002**, *14*, R285–R340.

[103] Xie, J.; Zhang, Y.; Yan, C. Y.; Song, L. N.; Wen, S.; Zang, F. C.; Chen, G.; Ding, Q.; Yan, C. Z.; Gu, N. High-performance PEGylated Mn–Zn ferrite nanocrystals as a passive-targeted agent for magnetically induced cancer theranostics. *Biomaterials* **2014**, *35*, 9126–9136.

[104] Lee, J. H.; Huh, Y. M.; Jun, Y. W.; Seo, J. W.; Jang, J. T.; Song, H. T.; Kim, S.; Cho, E. J.; Yoon, H. G.; Suh, J. S.; et al. Artificially engineered magnetic nanoparticles for ultra-sensitive molecular imaging. *Nat. Med.* **2007**, *13*, 95–99.

[105] Song, L. N.; Yan, C. Z.; Zhang, W.; Wu, H. A.; Jia, Z. Y.; Ma, M.; Xie, J.; Gu, N.; Zhang, Y. Influence of reaction solvent on Crystallinity and magnetic properties of $MnFe_2O_4$ nanoparticles synthesized by thermal decomposition. *J. Nanomater.* **2016**, *2016*, 4878935.

[106] Ge, Y. Q.; Zhang, Y.; Xia, J. G.; Ma, M.; He, S. Y.; Nie, F.; Gu, N. Effect of surface charge and agglomerate degree of magnetic iron oxide nanoparticles on KB cellular uptake *in vitro*. *Colloids Surf. B: Biointerf.* **2009**, *73*, 294–301.

[107] Xiong, F.; Yan, C. Y.; Tian, J. L.; Geng, K. K.; Zhu, Z. Y.; Song, L. N.; Zhang, Y.; Mulvale, M.; Gu, N. 2, 3-Dimercaptosuccinic acid-modified iron oxide clusters for magnetic resonance imaging. *J. Pharmaceut. Sci.* **2014**, *103*, 4030–4037.

[108] Zheng, X. W.; Chen, Y. J.; Wang, Z. M.; Song, L. N.; Zhang, Y.; Gu, N.; Xiong, F. Preparation and *in vitro* cellular uptake assessment of multifunctional Rubik-like magnetic Nano-assemblies. *J. Nanosci. Nanotechnol.* **2019**, *19*, 3301–3309.

[109] Butter, K.; Bomans, P. H. H.; Frederik, P. M.; Vroege, G. J.; Philipse, A. P. Direct observation of dipolar chains in iron ferrofluids by cryogenic electron microscopy. *Nat. Mater.* **2003**, *2*, 88–91.

[110] Gao, M. R.; Zhang, S. R.; Jiang, J.; Zheng, Y. R.; Tao, D. Q.; Yu, S. H. One-pot synthesis of hierarchical magnetite nanochain assemblies with complex building units and their application for water treatment. *J. Mater. Chem.* **2011**, *21*, 16888–16892.

[111] Hu, M. J.; Lu, Y.; Zhang, S.; Guo, S. R.; Lin, B.; Zhang, M.; Yu, S. H. High yield synthesis of bracelet-like hydrophilic Ni−Co magnetic alloy flux-closure Nanorings. *J. Am. Chem. Soc.* **2008**, *130*, 11606–11607.

[112] Wang, H.; Chen, Q. W.; Sun, Y. B.; Wang, M. S.; Sun, L. X.; Yan, W. S. Synthesis of necklace-like magnetic Nanorings. *Langmuir* **2010**, *26*, 5957–5962.

[113] Yang, F.; Zhang, X. X.; Song, L. N.; Cui, H. T.; Myers, J. N.; Bai, T. T.; Zhou, Y.; Chen, Z.; Gu, N. Controlled drug release and hydrolysis mechanism of polymer–magnetic nanoparticle composite. *ACS Appl. Mater. Interfaces* **2015**, *7*, 9410–9419.

[114] Lu, Y.; Zhao, Y.; Yu, L.; Dong, L.; Shi, C.; Hu, M. J.; Xu, Y. J.; Wen, L. P.; Yu, S. H. Hydrophilic Co@Au Yolk/Shell Nanospheres: Synthesis, assembly, and application to gene delivery. *Adv. Mater.* **2010**, *22*, 1407–1411.

[115] Sheparovych, R.; Sahoo, Y.; Motornov, M.; Wang, S. M.; Luo, H.; Prasad, P. N.; Sokolov, I.; Minko, S. Polyelectrolyte stabilized nanowires from Fe_3O_4 nanoparticles via magnetic field induced self-assembly. *Chem. Mater.* **2006**, *18*, 591–593.

[116] Fan, F. G.; Sun, J. F.; Chen, B.; Li, Y.; Hu, K.; Wang, P.; Ma, M.; Gu, N. Rotating magnetic field-controlled fabrication of magnetic hydrogel with spatially disk-like microstructures. *Sci. China Mater.* **2018**, *61*, 1112–1122.

[117] Sun, J. F.; Zhang, Y.; Chen, Z. P.; Zhou, J.; Gu, N. Fibrous aggregation of magnetite nanoparticles induced by a time-varied magnetic field. *Angew. Chem., Int. Ed.* **2007**, *46*, 4767–4770.

[118] Zhang, W. X.; Sun, J. F.; Bai, T. T.; Wang, C. Y.; Zhuang, K. H.; Zhang, Y.; Gu, N. Quasi-one-dimensional assembly of magnetic nanoparticles induced by a 50 Hz alternating magnetic field. *ChemPhysChem* **2010**, *11*, 1867–1870.

[119] Sun, J. F.; Su, Y. X.; Wang, C. Y.; Gu, N. The investigation of frequency response for the magnetic nanoparticulate assembly induced by time-varied magnetic field. *Nanoscale Res. Lett.* **2011**, *6*, 453.

[120] Guo, Z. B.; Hu, K.; Sun, J. F.; Zhang, T. Z.; Zhang, Q. Y.; Song, L. N.; Zhang, X. Z.; Gu, N. Fabrication of hydrogel with cell adhesive Micropatterns for mimicking the oriented tumor-associated extracellular matrix. *ACS Appl. Mater. Interfaces* **2014**, *6*, 10963–10968.

[121] Hu, K.; Zhou, N. Z.; Li, Y.; Ma, S. Y.; Guo, Z. B.; Cao, M.; Zhang, Q. Y.; Sun, J. F.; Zhang, T. Z.; Gu, N. Sliced magnetic polyacrylamide hydrogel with cell-adhesive microarray interface: A novel multi-cellular spheroid culturing platform. *ACS Appl. Mater. Interfaces* **2016**, *8*, 15113–15119.

[122] Sun, J. F.; Mao, Y. Q.; Guo, Z. R.; Zhang, Y.; Gu, N. Time-varied magnetic-field induced monolayer formation and re-aggregation of Au nanoparticles during solvent evaporation. *J. Nanosci. Nanotechnol.* **2009**, *9*, 1156–1159.

[123] Sun, J. F.; Dong, J.; Sun, D. K.; Guo, Z. R.; Gu, N. Magnetically mediated Vortexlike assembly of gold Nanoshells. *Langmuir* **2012**, *28*, 6520–6526.

[124] Perica, K.; Tu, A.; Richter, A.; Bieler, J. G.; Edidin, M.; Schneck, J. P. Magnetic field-induced T Cell receptor clustering by nanoparticles enhances T cell activation and stimulates antitumor activity. *ACS Nano* **2014**, *8*, 2252–2260.

[125] Guo, C.; Kaufman, L. J. Flow and magnetic field induced collagen alignment. *Biomaterials* **2007**, *28*, 1105–1114.

[126] Sun, J. F.; Zhou, H. Y.; Jin, Y. L.; Wang, M.; Li, Y. F.; Gu, N. Magnetically enhanced Dielectrophoretic assembly of horseradish peroxidase molecules: Chaining and molecular monolayers. *ChemPhysChem* **2008**, *9*, 1847–1850.

[127] Sun, J. F.; Sun, F.; Xu, B. B.; Gu, N. The quasi-one-dimensional assembly of horseradish peroxidase molecules in presence of the alternating magnetic field. *Colloids Surf. A: Physicochem. Eng. Aspects* **2010**, *360*, 94–98.

[128] Lu, Y.; Dong, L.; Zhang, L. C.; Su, Y. D.; Yu, S. H. Biogenic and biomimetic magnetic nanosized assemblies. *Nano Today* **2012**, *7*, 297–315.

[129] Kinge, S.; Crego-Calama, M.; Reinhoudt, D. N. Self-assembling nanoparticles at surfaces and interfaces. *ChemPhysChem* **2008**, *9*, 20–42.

[130] Fan, F. G.; Liu, J.; Sun, J. F.; Ma, S. Y.; Wang, P.; Gu, N. Magnetic energy-based understanding the mechanism of magnetothermal anisotropy for macroscopically continuous film of assembled Fe_3O_4 nanoparticles. *AIP Adv.* **2017**, *7*, 085109.

[131] Wang, P.; Sun, J. F.; Lou, Z. C.; Fan, F. G.; Hu, K.; Sun, Y.; Gu, N. Assembly-induced thermogenesis of gold nanoparticles in the presence of alternating magnetic field for controllable drug release of hydrogel. *Adv. Mater.* **2016**, *28*, 10801–10808.

[132] Guo, R.; Jiao, T. F.; Li, R. F.; Chen, Y.; Guo, W. C.; Zhang, L. X.; Zhou, J. X.; Zhang, Q. R.; Peng, Q. M. Sandwiched Fe_3O_4/Carboxylate Graphene oxide nanostructures constructed by layer-by-layer assembly for highly efficient and magnetically recyclable dye removal. *ACS Sustainable Chem. Eng.* **2018**, *6*, 1279–1288.

[133] Liu, X.; Zhang, J.; Tang, S. J.; Sun, J. F.; Lou, Z. C.; Yang, Y.; Wang, P.; Li, Y.; Gu, N. Growth enhancing effect of LBL-assembled magnetic nanoparticles on primary bone marrow cells. *Sci. China Mater.* **2016**, *59*, 901–910.

[134] Zierold, R.; Wu, Z. Y.; Biskupek, J.; Kaiser, U.; Bachmann, J.; Krill III, C. E.; Nielsch, K. Magnetic, multilayered nanotubes of low aspect ratios for liquid suspensions. *Adv. Funct. Mater.* **2011**, *21*, 226–232.

[135] Wang, C. G.; Irudayaraj, J. Multifunctional magnetic–optical nanoparticle probes for simultaneous detection, separation, and thermal ablation of multiple pathogens. *Small* **2010**, *6*, 283–289.

[136] Park, J. H.; von Maltzahn, G.; Zhang, L. L.; Schwartz, M. P.; Ruoslahti, E.; Bhatia, S. N.; Sailor, M. J. Magnetic iron oxide Nanoworms for tumor targeting and imaging. *Adv. Mater.* **2008**, *20*, 1630–1635.

[137] Kobayashi, M.; Seki, M.; Tabata, H.; Watanabe, Y.; Yamashita, I.

Fabrication of aligned magnetic nanoparticles using Tobamoviruses. *Nano Lett*. **2010**, *10*, 773–776.
[138] Hu, P.; Yu, L. J.; Zuo, A. H.; Guo, C. Y.; Yuan, F. L. Fabrication of Monodisperse magnetite hollow spheres. *J. Phys. Chem. C* **2009**, *113*, 900–906.
[139] Guan, N. N.; Wang, Y. T.; Sun, D. J.; Xu, J. A simple one-pot synthesis of single-crystalline magnetite hollow spheres from a single iron precursor. *Nanotechnology* **2009**, *20*, 105603.
[140] Liu, Z.; Lammers, T.; Ehling, J.; Fokong, S.; Bornemann, J.; Kiessling, F.; Gätjens, J. Iron oxide nanoparticle-containing microbubble composites as contrast agents for MR and ultrasound dual-modality imaging. *Biomaterials* **2011**, *32*, 6155–6163.
[141] Wang, N.; Cao, X.; Kong, D. S.; Chen, W. M.; Guo, L.; Chen, C. P. Nickel chains assembled by hollow microspheres and their magnetic properties. *J. Phys. Chem. C* **2008**, *112*, 6613–6619.
[142] Yang, F.; Chen, P.; He, W.; Gu, N.; Zhang, X. Z.; Fang, K.; Zhang, Y.; Sun, J. F.; Tong, J. Y. Bubble Microreactors triggered by an alternating magnetic field as diagnostic and therapeutic delivery devices. *Small* **2010**, *6*, 1300–1305.
[143] He, W.; Yang, F.; Wu, Y. H.; Wen, S.; Chen, P.; Zhang, Y.; Gu, N. Microbubbles with surface coated by superparamagnetic iron oxide nanoparticles. *Mater. Lett*. **2012**, *68*, 64–67.
[144] Duan, L.; Yang, F.; Song, L. N.; Fang, K.; Tian, J. L.; Liang, Y. J.; Li, M. X.; Xu, N.; Chen, Z. D.; Zhang, Y. et al. Controlled assembly of magnetic nanoparticles on microbubbles for multimodal imaging. *Soft Matter* **2015**, *11*, 5492–5500.
[145] Fang, K.; Song, L. N.; Gu, Z. X.; Yang, F.; Zhang, Y.; Gu, N. Magnetic field activated drug release system based on magnetic PLGA microspheres for chemo-thermal therapy. *Colloids Surf. B: Biointerf*. **2015**, *136*, 712–720.
[146] Yang, F.; Li, Y. X.; Chen, Z. P.; Gu, N. The preparation and application of microbubble contrast agent combining ultrasound imaging and magnetic resonance imaging. *Chin. Sci. Bull*. **2009**, *54*, 2934–2939.
[147] Yang, F.; Li, M. X.; Liu, Y.; Wang, T. T.; Feng, Z. Q.; Cui, H. T.; Gu, N. Glucose and magnetic-responsive approach toward *in situ* nitric oxide bubbles controlled generation for hyperglycemia theranostics. *J. Controlled Release* **2016**, *228*, 87–95.
[148] Soetanto, K.; Watarai, H. Development of magnetic Microbubbles for Drug Delivery System (DDS). *Jpn. J. Appl. Phys*. **2000**, *39*, 3230–3232.
[149] Poehlmann, M.; Grishenkov, D.; Kothapalli, S. V. V. N.; Härmark, J.; Hebert, H.; Philipp, A.; Hoeller, R.; Seuss, M.; Kuttner, C.; Margheritelli, S. et al. On the interplay of shell structure with low- and high-frequency mechanics of multifunctional magnetic microbubbles. *Soft Matter* **2014**, *10*, 214–226.
[150] Hou, M.; Chen, C. X.; Tang, D. L.; Luo, S. H.; Yang, F.; Gu, N. Magnetic microbubble-mediated ultrasound-MRI registration based on robust optical flow model. *Biomed. Eng. Online* **2015**, *14 Suppl 1*, S14.
[151] Li, M. X.; Li, J.; Chen, J. P.; Liu, Y.; Cheng, X.; Yang, F.; Gu, N. Platelet membrane biomimetic magnetic Nanocarriers for targeted delivery and *in situ* generation of nitric oxide in early ischemic stroke. *ACS Nano* **2020**, *14*, 2024–2035.
[152] Liu, Y.; Yang, F.; Yuan, C. X.; Li, M. X.; Wang, T. T.; Chen, B.; Jin, J.; Zhao, P.; Tong, J. Y.; Luo, S. H. et al. Magnetic Nanoliposomes as *in situ* Microbubble bombers for multimodality image-guided cancer Theranostics. *ACS Nano* **2017**, *11*, 1509–1519.
[153] Zhou, Y.; Gu, N.; Yang, F. *In situ* microbubble-assisted, ultrasound-controlled release of superparamagnetic iron oxide nanoparticles from gastro-retentive tablets. *Int. J. Pharm*. **2020**, *586*, 119615.
[154] Yang, F.; Li, M. X.; Cui, H. T.; Wang, T. T.; Chen, Z. W.; Song, L. N.; Gu, Z. X.; Zhang, Y.; Gu, N. Altering the response of intracellular reactive oxygen to magnetic nanoparticles using ultrasound and microbubbles. *Sci. China Mater*. **2015**, *58*, 467–480.
[155] Yang, F.; Zhang, M.; He, W.; Chen, P.; Cai, X. W.; Yang, L.; Gu, N.; Wu, J. R. Controlled release of Fe_3O_4 nanoparticles in encapsulated Microbubbles to tumor cells via Sonoporation and associated cellular Bioeffects. *Small* **2011**, *7*, 902–910.
[156] Li, J.; Feng, Z. Q.; Gu, N.; Yang, F. Superparamagnetic iron oxide nanoparticles assembled magnetic nanobubbles and their application for neural stem cells labeling. *J. Mater. Sci. Technol*. **2021**, *63*, 124–132.
[157] Kircher, M. F.; Willmann, J. K. Molecular body imaginG: MR imaging, CT, and US. Part I. Principles. *Radiology* **2012**, *263*, 633–643.
[158] Chen, Y. J.; Tao, J.; Xiong, F.; Zhu, J. B.; Gu, N.; Zhang, Y. H.; Ding, Y.; Ge, L. Synthesis, self-assembly, and characterization of PEG-coated iron oxide nanoparticles as potential MRI contrast agent. *Drug Dev. Ind. Pharm*. **2010**, *36*, 1235–1244.
[159] Chen, Y. J.; Chen, Y. J.; Tao, J.; Tao, J.; Xiong, F.; Zhu, J. B.; Gu, N.; Geng, K. K.; Geng, K. K. Characterization and *in vitro* cellular uptake of PEG coated iron oxide nanoparticles as MRI contrast agent. *Die Pharm. - An Int. J. Pharm. Sci*. **2010**, *65*, 481–486.
[160] Wang, J. D.; Xie, J.; Zhou, X. J.; Cheng, Z.; Gu, N.; Teng, G. J.; Hu, Q. J.; Zhu, F. P.; Chang, S. H.; Zhang, F.; et al. Ferritin enhances SPIO tracking of C6 rat glioma cells by MRI. *Mol. Imaging Biol*. **2011**, *13*, 87–93.
[161] Song, L. N.; Zang, F. C.; Song, M. J.; Chen, G.; Zhang, Y.; Gu, N. Effective PEGylation of Fe_3O_4 Nanomicelles for *in vivo* MR imaging. *J. Nanosci. Nanotechnol*. **2015**, *15*, 4111–4118.
[162] Lee, N.; Choi, Y.; Lee, Y.; Park, M.; Moon, W. K.; Choi, S. H.; Hyeon, T. Water-dispersible Ferrimagnetic iron oxide Nanocubes with extremely High r_2 Relaxivity for highly sensitive *in vivo* MRI of tumors. *Nano Lett*. **2012**, *12*, 3127–3131.
[163] Brooks, R. A.; Moiny, F.; Gillis, P. On T_2-shortening by weakly magnetized particles: The chemical exchange model. *Magn. Reson. Med*. **2001**, *45*, 1014–1020.
[164] Lee, S. H.; Kim, B. H.; Na, H. B.; Hyeon, T. Paramagnetic inorganic nanoparticles as T_1 MRI contrast agents. *WIREs Nanomed. Nanobiotechnol*. **2014**, *6*, 196–209.
[165] Kim, B. H.; Lee, N.; Kim, H.; An, K.; Park, Y. I.; Choi, Y.; Shin, K.; Lee, Y.; Kwon, S. G.; Na, H. B. et al. Large-scale synthesis of uniform and extremely small-sized iron oxide nanoparticles for high-resolution T_1 magnetic resonance imaging contrast agents. *J. Am. Chem. Soc*. **2011**, *133*, 12624–12631.
[166] Wang, Z. Y.; Liu, J.; Li, T. R.; Liu, J.; Wang, B. D. Controlled synthesis of $MnFe_2O_4$ nanoparticles and Gd complex-based nanocomposites as tunable and enhanced T_1/T_2-weighted MRI contrast agents. *J. Mater. Chem. B* **2014**, *2*, 4748–4753.
[167] Penfield, J. G.; Reilly, R. F. Jr. What nephrologists need to know about gadolinium. *Nat. Clin. Pract. Nephrol*. **2007**, *3*, 654–668.
[168] Caravan, P. Strategies for increasing the sensitivity of gadolinium based MRI contrast agents. *Chem. Soc. Rev*. **2006**, *35*, 512–523.
[169] Chen, L.; Zang, F. C.; Wu, H. A.; Li, J. Z.; Xie, J.; Ma, M.; Gu, N.; Zhang, Y. Using PEGylated magnetic nanoparticles to describe the EPR effect in tumor for predicting therapeutic efficacy of micelle drugs. *Nanoscale* **2018**, *10*, 1788–1797.
[170] Xia, Y.; Sun, J. F.; Zhao, L.; Zhang, F. M.; Liang, X. J.; Guo, Y.; Weir, M. D.; Reynolds, M. A.; Gu, N.; Xu, H. H. K. Magnetic field and nano-scaffolds with stem cells to enhance bone regeneration. *Biomaterials* **2018**, *183*, 151–170.
[171] Tian, J.; Yan, C. Y.; Liu, K. L.; Tao, J.; Guo, Z. C.; Liu, J. P.; Zhang, Y.; Xiong, F.; Gu, N. Paclitaxel-loaded magnetic nano-particles: Synthesis, characterization, and application in targeting. *J. Pharmaceut. Sci*. **2017**, *106*, 2115–2122.
[172] Lee, I. S.; Lee, N.; Park, J.; Kim, B. H.; Yi, Y. W.; Kim, T.; Kim, T. K.; Lee, I. H.; Paik, S. R.; Hyeon, T. Ni/NiO core/shell nanoparticles for selective binding and magnetic separation of Histidine-tagged proteins. *J. Am. Chem. Soc*. **2006**, *128*, 10658–10659.
[173] Kim, J.; Tran, V. T.; Oh, S.; Kim, C. S.; Hong, J. C.; Kim, S.; Joo, Y. S.; Mun, S.; Kim, M. H.; Jung, J. W. et al. Scalable Solvothermal synthesis of Superparamagnetic Fe_3O_4 Nanoclusters for Bioseparation and Theragnostic probes. *ACS Appl. Mater. Interfaces* **2018**, *10*, 41935–41946.
[174] Lim, J.; Dobson, J. Improved transfection of HUVEC and MEF cells using DNA complexes with magnetic nanoparticles in an oscillating field. *J. Genet*. **2012**, *91*, 223–227.
[175] Gersting, S. W.; Schillinger, U.; Lausier, J.; Nicklaus, P.; Rudolph, C.; Plank, C.; Reinhardt, D.; Rosenecker, J. Gene delivery to respiratory epithelial cells by magnetofection. *J. Gene Med*. **2004**, *6*, 913–922.

[176] Krötz, F.; Sohn, H. Y.; Gloe, T.; Plank, C.; Pohl, U. Magnetofection potentiates gene delivery to cultured endothelial cells. *J. Vasc. Res.* **2003**, *40*, 425–434.
[177] Liang, Y. J.; Wang, H. Y.; Yu, H.; Feng, G. D.; Liu, F.; Ma, M.; Zhang, Y.; Gu, N. Magnetic navigation helps PLGA drug loaded magnetic microspheres achieve precise chemoembolization and hyperthermia. *Colloids Surf. A: Physicochem. Eng. Aspects* **2020**, *588*, 124364.
[178] Liu, Y.; Li, J.; Chen, H. M.; Cai, Y.; Sheng, T. Y.; Wang, P.; Li, Z. Y.; Yang, F.; Gu, N. Magnet-activatable nanoliposomes as intracellular bubble microreactors to enhance drug delivery efficacy and burst cancer cells. *Nanoscale* **2019**, *11*, 18854–18865.
[179] Dames, P.; Gleich, B.; Flemmer, A.; Hajek, K.; Seidl, N.; Wiekhorst, F.; Eberbeck, D.; Bittmann, I.; Bergemann, C.; Weyh, T. et al. Targeted delivery of magnetic aerosol droplets to the lung. *Nat. Nanotechnol.* **2007**, *2*, 495–499.
[180] Cai, Q. D.; Mai, X. L.; Miao, W. L.; Zhou, X.; Zhang, Y.; Liu, X.; Lu, W.; Zhang, J. Q.; Gu, N.; Sun, J. F. Specific, Non-invasive, and magnetically directed targeting of magnetic erythrocytes in blood vessels of Mice. *IEEE Trans. Biomed. Eng.* **2020**, *67*, 2276–2285.
[181] Liang, Y. J.; Yu, H.; Feng, G. D.; Zhuang, L. L.; Xi, W.; Ma, M.; Chen, J.; Gu, N.; Zhang, Y. High-performance Poly(lactic-co-glycolic acid)-Magnetic microspheres prepared by rotating membrane emulsification for Transcatheter arterial embolization and magnetic ablation in VX_2 Liver Tumors. *ACS Appl. Mater. Interfaces* **2017**, *9*, 43478–43489.
[182] Wang, G. H.; Xu, D. R.; Chai, Q.; Tan, X. L.; Zhang, Y.; Gu, N.; Tang, J. T. Magnetic fluid hyperthermia inhibits the growth of breast carcinoma and downregulates vascular endothelial growth factor expression. *Oncol. Lett.* **2014**, *7*, 1370–1374.
[183] Benyettou, F.; Das, G.; Nair, A. R.; Prakasam, T.; Shinde, D. B.; Sharma, S. K.; Whelan, J.; Lalatonne, Y.; Traboulsi, H.; Pasricha, R. et al. Covalent organic framework embedded with magnetic nanoparticles for MRI and chemo-thermotherapy. *J. Am. Chem. Soc.* **2020**, *142*, 18782–18794.
[184] Song, Y. H.; Li, D. D.; Lu, Y.; Jiang, K.; Yang, Y.; Xu, Y. J.; Dong, L.; Yan, X.; Ling, D. S.; Yang, X. Z. et al. Ferrimagnetic mPEG-*b*-PHEP copolymer micelles loaded with iron oxide nanocubes and emodin for enhanced magnetic hyperthermia–chemotherapy. *Natl. Sci. Rev.* **2020**, *7*, 723–736.
[185] Ma, M.; Zhang, Y.; Gu, N. Estimation the tumor temperature in magnetic nanoparticle hyperthermia by infrared thermography: Phantom and numerical studies. *J. Therm. Biol.* **2018**, *76*, 89–94.
[186] Polo-Corrales, L.; Rinaldi, C. Monitoring iron oxide nanoparticle surface temperature in an alternating magnetic field using thermoresponsive fluorescent polymers. *J. Appl. Phys.* **2012**, *111*, 07B334.
[187] Xu, R. Z.; Zhang, Y.; Ma, M.; Xia, J. G.; Liu, J. W.; Guo, Q. Z.; Gu, N. Measurement of specific absorption rate and thermal simulation for arterial embolization hyperthermia in the Maghemite-gelled model. *IEEE Trans. Magnet.* **2007**, *43*, 1078–1085.
[188] Xu, R. Z.; Yu, H.; Zhang, Y.; Ma, M.; Chen, Z. P.; Wang, C. L.; Teng, G. J.; Ma, J.; Sun, X. C.; Gu, N. Three-dimensional model for determining inhomogeneous thermal dosage in a liver tumor during arterial embolization hyperthermia incorporating magnetic nanoparticles. *IEEE Trans. Magnet.* **2009**, *45*, 3085–3091.
[189] Ma, M.; Zhang, Y.; Shen, X. L.; Xie, J.; Li, Y.; Gu, N. Targeted inductive heating of nanomagnets by a combination of alternating current (AC) and static magnetic fields. *Nano Res.* **2015**, *8*, 600–610.
[190] Qian, K. Y.; Song, Y. H.; Yan, X.; Dong, L.; Xue, J. Z.; Xu, Y. J.; Wang, B.; Cao, B. Q.; Hou, Q. B.; Peng, W. et al. Injectable ferrimagnetic silk fibroin hydrogel for magnetic hyperthermia ablation of deep tumor. *Biomaterials* **2020**, *259*, 120299.
[191] Zhang, X. Q.; Gong, S. W.; Zhang, Y.; Yang, T.; Wang, C. Y.; Gu, N. Prussian blue modified iron oxide magnetic nanoparticles and their high peroxidase-like activity. *J. Mater Chem.* **2010**, *20*, 5110–5116.
[192] Chen, Z. W.; Yin, J. J.; Zhou, Y. T.; Zhang, Y.; Song, L. N.; Song, M. J.; Hu, S. L.; Gu, N. Dual enzyme-like activities of iron oxide nanoparticles and their implication for diminishing cytotoxicity. *ACS Nano* **2012**, *6*, 4001–4012.
[193] Dowding, J. M.; Dosani, T.; Kumar, A.; Seal, S.; Self, W. T. Cerium oxide nanoparticles scavenge nitric oxide radical (˙NO). *Chem. Commun.* **2012**, *48*, 4896–4898.
[194] Dong, J. L.; Song, L. N.; Yin, J. J.; He, W. W.; Wu, Y. H.; Gu, N.; Zhang, Y. Co_3O_4 Nanoparticles with multi-enzyme activities and their application in Immunohistochemical assay. *ACS Appl. Mater. Interfaces* **2014**, *6*, 1959–1970.
[195] Zhang, W.; Zhang, Y.; Chen, Y. H.; Li, S. Y.; Gu, N.; Hu, S. L.; Sun, Y.; Chen, X.; Li, Q. Prussian blue modified ferritin as peroxidase Mimetics and its applications in biological detection. *J. Nanosci. Nanotechnol.* **2013**, *13*, 60–67.
[196] Zhang, W.; Hu, S. L.; Yin, J. J.; He, W. W.; Lu, W.; Ma, M.; Gu, N.; Zhang, Y. Prussian blue nanoparticles as Multienzyme Mimetics and reactive oxygen species scavengers. *J. Am. Chem. Soc.* **2016**, *138*, 5860–5865.
[197] Zhang, W.; Wu, Y.; Dong, H. J.; Yin, J. J.; Zhang, H.; Wu, H. A.; Song, L. N.; Chong, Y.; Li, Z. X.; Gu, N. et al. Sparks fly between ascorbic acid and iron-based nanozymes: A study on Prussian blue nanoparticles. *Colloids Surf. B: Biointerf.* **2018**, *163*, 379–384.
[198] Peng, F. F.; Zhang, Y.; Gu, N. Size-dependent peroxidase-like catalytic activity of Fe_3O_4 nanoparticles. *Chin. Chem. Lett.* **2008**, *19*, 730–733.
[199] Ma, M.; Xie, J.; Zhang, Y.; Chen, Z. P.; Gu, N. Fe_3O_4@Pt nanoparticles with enhanced peroxidase-like catalytic activity. *Mater. Lett.* **2013**, *105*, 36–39.
[200] Song, L. N.; Huang, C.; Zhang, W.; Ma, M.; Chen, Z. W.; Gu, N.; Zhang, Y. Graphene oxide-based Fe_2O_3 hybrid enzyme mimetic with enhanced peroxidase and catalase-like activities. *Colloids Surf. A: Physicochem. Eng. Aspects* **2016**, *506*, 747–755.
[201] Fan, K. L.; Wang, H.; Xi, J. Q.; Liu, Q.; Meng, X. Q.; Duan, D. M.; Gao, L. Z.; Yan, X. Y. Optimization of Fe_3O_4 nanozyme activity via single amino acid modification mimicking an enzyme active site. *Chem. Commun.* **2017**, *53*, 424–427.
[202] Wei, H.; Wang, E. K. Nanomaterials with enzyme-like characteristics (nanozymes): Next-generation artificial enzymes. *Chem. Soc. Rev.* **2013**, *42*, 6060–6093.
[203] Yang, F.; Hu, S. L.; Zhang, Y.; Cai, X. W.; Huang, Y.; Wang, F.; Wen, S.; Teng, G. J.; Gu, N. A hydrogen peroxide-responsive O_2 Nanogenerator for ultrasound and magnetic-resonance dual modality imaging. *Adv. Mater.* **2012**, *24*, 5205–5211.
[204] Wu, H. A.; Liu, L.; Song, L. N.; Ma, M.; Gu, N.; Zhang, Y. Enhanced tumor synergistic therapy by injectable magnetic hydrogel mediated generation of hyperthermia and highly toxic reactive oxygen species. *ACS Nano* **2019**, *13*, 14013–14023.
[205] Sun, Y. X.; Shi, F. F.; Niu, Y. J.; Zhang, Y.; Xiong, F. Fe_3O_4@OA@Poloxamer nanoparticles lower triglyceride in hepatocytes through liposuction effect and nano-enzyme effect. *Colloids Surf. B: Biointerf.* **2019**, *184*, 110528.
[206] Vernekar, A. A.; Sinha, D.; Srivastava, S.; Paramasivam, P. U.; D'Silva, P.; Mugesh, G. An antioxidant nanozyme that uncovers the cytoprotective potential of vanadia nanowires. *Nat. Commun.* **2014**, *5*, 5301.